DEFECT STUDIES IN Cu-BASED P-TYPE TRANSPARENT CONDUCTING OXIDES

by

FNU AMEENA

Presented to the Faculty of the Graduate School of

The University of Texas at Arlington in Partial Fulfillment

of the Requirements

for the Degree of

DOCTOR OF PHILOSOPHY

THE UNIVERSITY OF TEXAS AT ARLINGTON

May 2012

ACKNOWLEDGEMENTS

I am greatly honored to have the opportunity to express my sincere appreciation to all those people who supported me during my Ph.D. program at the University of Texas at Arlington.

First and foremost I would like to express my best gratitude and appreciation to my research advisor, Dr. Michael Jin, for his constant support, guidance and encouragement throughout my Ph. D study. Without his support and patience this research would not be finished. He taught many things which are unforgettable both as a researcher and as a person which will remain in my heart and benefit my whole life.

I am truly thankful to Dr. C. A. Quarles, Professor at Texas Christian University and our collaborator without whom I could not finish my experiments which are very crucial in this research. The knowledge he shared and the advice he gave me during my experiments helped me in finishing up my dissertation. I would also like to sincerely thank all my committee members Dr. Alex H. Weiss, Dr. Nail Fazleev, Dr. Qiming Zhang and Dr. E. I. Meletis for their useful discussions, advice and comments during this research work.

I also want to express my special thanks to my former and current group members: Mr. Eray Erkin, Mr. Soo Kim, Mr. Alex Huang, Mr. Yacob, Mr. Daniel Wu, Mr. Clement, Mr. Alex and Mr. Yi Yang for their help and support throughout my research. The moments we shared together, the laughter we had, I will definitely remember them as my beautiful times in my life.

I want to thank the staff members of Characterization center of materials and biology , Dr. Jiang and Mr. David for their assistance in using the characterization tools. I owe a special note of thanks to staff members Jennifer Standlee, Libia Cuauhtli, Margie Jackymack for their constant help and encouragement throughout my life at UTA.

Finally, without the constant support and love from my husband, Laxmi Nimma, and my dearest son Abhiram who is my inspiration, my parents who always gave me the spirit of never giving up and stood by me during my hard times, my brothers and all my dear friends, it could have been impossible to achieve my Ph.D study. I would like to express my sincere thanks to all of them.

December 15, 2011

ABSTRACT

DEFECT STUDIES IN Cu-BASED P-TYPE TRANSPARENT CONDUCTING OXIDES

FNU AMEENA, PhD

The University of Texas at Arlington, 2012

Supervising Professor: Michael Jin

Among other intrinsic open-volume defects, copper vacancy (V_{Cu}) has been theoretically identified as the major acceptor in p-type Cu-based semiconducting transparent oxides, which has potential as low-cost photovoltaic absorbers in semi-transparent solar cells. A series of positron annihilation experiments with pure Cu, Cu_2O, and CuO presented strong presence of V_{Cu} and its complexes in the copper oxides. The lifetime data also showed that the density of V_{Cu} was becoming higher as the oxidation state of Cu increased which was consistent with the decrease in the formation energy of V_{Cu}. Doppler broadening measurements further indicated that electrons with low momentum made more contribution to the contributed as pure Cu oxidizes to copper oxides.

The metastable defects are known to be generated in Cu_2O upon illumination and it has been known to affect the performance of Cu_2O-based hetero-junctions used in solar cells. The metastable effect was studied using positron annihilation lifetime spectroscopy and its data showed the change in the defect population upon light exposure and the minimal effect of light-induced electron density increase in the bulk of materials to the average lifetime of the

positrons. The change in the defect population is concluded to be related to the dissociation and association of V_{Cu} – V_{Cu} complexes. For example, the shorter lifetime under light was ascribed to the annihilation with smaller size vacancies, which explains the dissociation of the complexes with light illumination. Doppler broadening of the annihilation was independent of light illumination, which suggested that the chemical nature of the defects remained without change upon their dissociation and association – only the size distribution of copper vacancies varied.

The delafossite metal oxides, $CuM^{III}O_2$ are emerging wide-bandgap p-type semiconductors. In this research, the formation energies of structural vacancies are calculated using Van Vechten cavity model as an attempt to study the effect of the size of the M^{III} cation in the delafossites starting from Cu_2O. Comparison of the formation energies between Cu_2O and delafossite oxides clearly showed that the equilibrium concentration of the vacancies depended strongly on the structural parameters varied by the presence of different M^{III} cations. In particular, the size of the M^{III} cation greatly influenced the defect formation energies of $V_{Cu.}$ It was observed from our calculations, as the size increases the formation energy decreases.

TABLE OF CONTENTS

ACKNOWLEDGEMENTS iii

ABSTRACT iv

LIST OF ILLUSTRATIONS vii

LIST OF TABLES viii

Chapter Page

1. INTRODUCTION 1

1.1 Research objective 1

1. 2 Overview of TCOs 2

1.2.1 Introduction to TCOs 2

1.2.2 n-type TCOs vs p-type TCOs 3

1.2.3 Cu-based p-type TCOs 7

1.3 Intrinsic defects in Cu-based p-type TCOs and the scope of research 9

1.3.1 Chemical identification of defects in Cu_2O 9

1.3.2 Light induced metastable defects in Cu_2O 10

1.3.3 Defect formation energies of intrinsic defects in Cu-based TCOs 11

2. EXPERIMENTAL TECHNIQUES AND MATERIALS 13

2.1 Experimental Techniques 13

2.1.1 Positron Annihilation Spectroscopy (PAS) 13

2.1.1.1 Introduction 13

2.1.1.2 Positron sources and its decay scheme 13

2.1.1.3 Principles 14

2.1.1.4 Positron lifetime measurements 15

2.1.1.5 Data Analysis 17

2.1.2 Doppler Broadening Spectroscopy (DBS) 19

2.1.2.1 Principle and Experimental set-up 19

2.1.2.2 Data Analysis 21

2.2 Materials 22

3. POSITRON ANNIHILATION IN COPPER OXIDES AND ITS DOPPLER BROADENING: CONNOTATION OF OXIDIZING Cu AND THE PRESENCE OF Cu VACANCIES 29

3.1 Introduction 29

3.2 Experiments 30

3.3 Results and Discussion 31

3.4 Summary 37

4. LIGHT-INDUCED METASTABLE DEFECTS IN Cu2O STUDIED BY POSITRON ANNIHILATION SPECTROSCOPY 38

4.1 Introduction 38

4.2 Background 39

4.2.1 Defect complex model 39

4.2.2 Electronic models 40

4.2.3 Acceptor-Donor complex model to explain PPC effects 42

4.3 Hypothesis and the design of experiments 47

4.4 Results and Discussions 48

4.5 Summary 52

5. INTRINSIC DEFECT STUDY IN Cu-BASED TRANSPARENT CONDUCTINGOXIDES 54

5.1 Introduction 54

5.2 Theory of VVCM 56

5.2.1 Introduction 56

5.2.2 Surface plasmon theory to determine E_s^m 57

5.2.3 Penn-Philips model to determine E^b 58
5.3 Calculations of Wigner-Seitz radii 59
5.4 Results and Discussion 62
5.5 Summary 68
6. CONCLUSIONS AND FUTURE WORK 69
6.1 Conclusions 69
6.2 Future work 70
REFERENCES 72
BIOGRAPHICAL INFORMATION 78

LIST OF ILLUSTRATIONS

Figure Page

1.1 2011 quarterly worldwide FPD annual forecast reports 3

1.2 (a) The band structure of ZnO showing that conduction band minimum (CBM) is formed mainly by metal s orbitals and valence band maximum (VBM) is formed by oxygen 2p orbitals (b) wave functions calculated by the density functional theory of the CBM(c)wave functions representing the VBM 4

1.3 Illustration showing the principle of chemical modulation of valence band (CMVB). The top of the valence band consists of cation d and oxygen 2p orbitals. The energy of the closed shell cations are assumed to be the same as that of oxygen 2p electrons 5

1.4 The energy band diagram obtained from photoemission spectra shows the valence band maximum (VBM) (red) and the conduction-band minimum (CBM) (blue) of TCOs. Inset (b) shows the blue emission from a ZnO p-n junction LED 6

1.5 (a) Cubic crystal structure of Cu_2O, grey atoms are Cu and black are O atoms (b) Delafossite crystal structure of $CuM^{III}O_2$, black atoms are O, dark grey and light grey atoms are M^{III} and Cu respectively 8

2.1 Decay scheme of the radioactive isotope 14

2.2 Typical scheme of positron experiments 15

2.3 (a) Experimental set-up to measure positron lifetime (b) Sandwich arrangement for sample positron source 16

2.4 Example showing a positron lifetime spectrum of as-grown Si (Czochralski-grown) and plastically deformed Si showing a bulk lifetime of 160ps and defect lifetimes of 320ps and 520ps 19

2.5 Experimental setup for measuring Doppler broadening spectrum 21

2.6 DBS for GaAs sample, triangles show the defect free sample and circles show the plastically deformed sample. A_s gives the area under curve of the low momentum parameter and A_w gives the area under the curve of the high momentum parameter 22

2.7 (a) SEM image of as-received Cu_2O at 10K magnification
(b) SEM image of as-received at 2.37K magnification 23

2.8 SEM image of as-received CuO 24

2.9 XRD of Cu_2O before annealing 26

2.10 XRD of Cu_2O after annealing 27

2.11 XRD of CuO 28

3.1 Room temperature PL measurements of Cu_2O 33

3.2 S-W plot of the Cu_2O, CuO and Cu disk 34

3.3 (a) Normalized DBS spectra of Cu,Cu_2O and CuO
(b) Ratio of the Normalized spectra of copper oxides to pure Cu 36

4.1 Proposed energy level diagram for Cu_2O.
The lowest level is an acceptor level and the two higher levels are trap levels 41

4.2 Electronic model proposed by Strasbourg group 42

4.3 Hole concentration as a function of temperature 43

4.4 PPC decay of Cu_2O under the dark as a function of time at three different temperatures 44

4.5 Representation of defect electronic levels using acceptor-donor complex model 46

4.6 DBS spectra before and after illumination 52

5.1 Dispersion relation for bulk solid with two branches of surface plasmon modes showing how the surface energy changes before splitting the crystal into two and after with respect to the plasmon modes 57

5.2 Electronic band structure based on Penn-Philips model showing the energy($E_g/4E_f$) of the idealized semiconductor 59

5.3 Crystal structure of Cu_2O along with the shapes of vacancy cavities of Cu-octahedron and O-tetrahedron 61

5.4 Crystal structures of delafossites along with the vacancy cavities of Cu-dodecahedron, O- tetrahedron and M^{III}-octahedron 62

LIST OF TABLES

Table Page

1.1 Defect formation energies of various Cu-based oxides along with the ionization energies from the literature 12

2.1 EDS compositional analysis on Cu_2O before annealing 25

3.1 Positron annihilation parameters, the defect and the bulk LT values and the S, W parameters for copper disk and copper oxide samples 32

4.1 Acceptor concentration, N_A, ionized donor concentration, N_D^+, and acceptor energy level, E_A obtained from the fit of p(T) using equation 4.1 41

4.2 PPC decay times for three samples at different temperatures 45

4.3 LT values from S1, S2 and S3 with a fixed bulk LT 49

4.4 Two LT values from S1, S2 and S3 without fixing any LT 50

4.5 Three LT values from S1, S2 and S3 without fixing any LT 51

5.1 Structural information of Cu_2O and delafossites from the literature. 60

5.2 Calculated defect formation energies of vacancies in Cu-based oxides. 63

5.3 Calculated E_g and E_F values according to the dielectric constants from the literature 64

5.4 The theoretically calculated effective hole masses of $CuInO_2$, $CuCrO_2$ and $CuAlO_2$ in the units of free electron mass along [100], [010] and [001] planes 66

5.5 Bader partial electron charges for $CuCrO_2$, $CuInO_2$ and $CuAlO_2$ calculated using LDA 67

5.6 Formation energies of Cu vacancies in $CuAlO_2$, $CuCrO_2$ and $CuInO_2$ calculated using LDA in comparison with the calculated results obtained in this study using VVCM 67

CHAPTER 1

INTRODUCTION

1.1 Research Objective

The objective of this thesis is to understand intrinsic defects of Cu-based p-type transparent conducting oxides (TCOs). We investigated critical questions in the field of p-type TCO materials by identifying the defects present. In the photovoltaic hetero-junctions made of the intrinsic p-type TCOs, the formation and ionization energies of intrinsic point defects become important since they determine much part of the equilibrium charge carrier concentration in the material, junction properties, and the recombination of photo-generated carriers. There are a number of theoretical studies those have predicted copper vacancies (V_{Cu}) to be major acceptors in all p-type Cu-based TCOs due to their low formation energies and ionization energies [1, 2]. To start with, we chose to identify the defects present in Cu_2O since it makes itself an interesting material due to its simple structure and forms a basic parent material to understand the defects in other ternary p-type TCO materials, here in our case delafossites with a chemical formula ($CuM^{III}O_2$). There is also a lively debate going on the possibility of synthesizing intrinsically n-type Cu_2O under acidic environment [3, 4], which further questions the chemical identity of the major point defects in Cu_2O in general. In this work, positron annihilation lifetime spectroscopy (PALS) [5, 6] in conjunction with Doppler broadening spectroscopy (DBS) and photoluminescence (PL) spectroscopy were performed to identify the major defects in Cu_2O. Another interest phenomenon of Cu_2O is the thermally activated persistent photo conductivity (PPC) [7-9], in which the high conductivity state of Cu_2O created by its exposure to light for a short period of time can prolong days under dark at room temperature. The presence of the metastable complexes in Cu_2O was revealed by PALS and DBS in this study in order to explain PPC. Fundamental understanding of structural defects in

Cu-based delafossite materials is important for realizing their potential as intrinsic p-type semiconductors. In particular, the equilibrium concentration of free charge carriers contributed from the defects is the major interest in this study. We calculated the defect formation energies of Cu-based delafossites and Cu_2O using Van Vechten Cavity model (VVCM) to see the effect of electronic structure on them. The study discusses how the defect formation energies depend on the size of the M^{III} cation, bond length between Cu-Cu atom, and the covalency in the compounds.

1.2 Overview of TCOs

1.2.1 Introduction to TCOs

TCO materials are remarkably interesting due to the combination of high conductivity in the order of 10^{-4} Ω·cm and high transparency in the visible spectrum. The band gap is generally as large as 3~4 eV and their properties can be exploited in several applications - transparent electrodes for photovoltaic cells and flat panel displays (FPD), optical coating in low-emissivity windows, electro-chromic windows, touch-sensitive control panels, and defrosting windows in vehicles [10-17]. Badekar et al [10] discovered CdO as the first TCO thin film with an optical band gap of 2.3 eV and a transparency of over 85 % in the visible spectrum and a resistivity of 2~5 x 10^{-4} Ω·cm [18]. Other examples of TCO thin films such as ZnO, SnO_2, and In_2O_3 were discovered later [19]. Making these applications often requires the exploration and the synthesis of new n-type and p-type TCO materials. Usually doping in TCO can be achieved by fabricating them with a non-stoichiometric composition or by introducing extrinsic dopants. Doping oxides results in increasing the electrical conductivity and most common doped-TCOs include Al-doped ZnO, Sn-doped In_2O_3 (ITO), and Sb- or F-doped SnO_2 (FTO) [19]. The current TCO industry is in scarcity of the resource materials since most dominant applications including (Flat Panel Displays) FPDs and architectural applications utilize much ITO and FTO materials. For example, the annual consumption of TCO coated glass primarily for low emissivity coatings in the United States was 7.3×10^7 m^2 or >27 mi^2 in 2004 [20]. The volume of FPDs produced

and the volume of ITO coatings produced continue to grow rapidly. The market for FPDs in 2011 is estimated to be over $125 billion and is predicted to be over $150 billion by 2015. The forecast of market size is shown in Fig. 1.

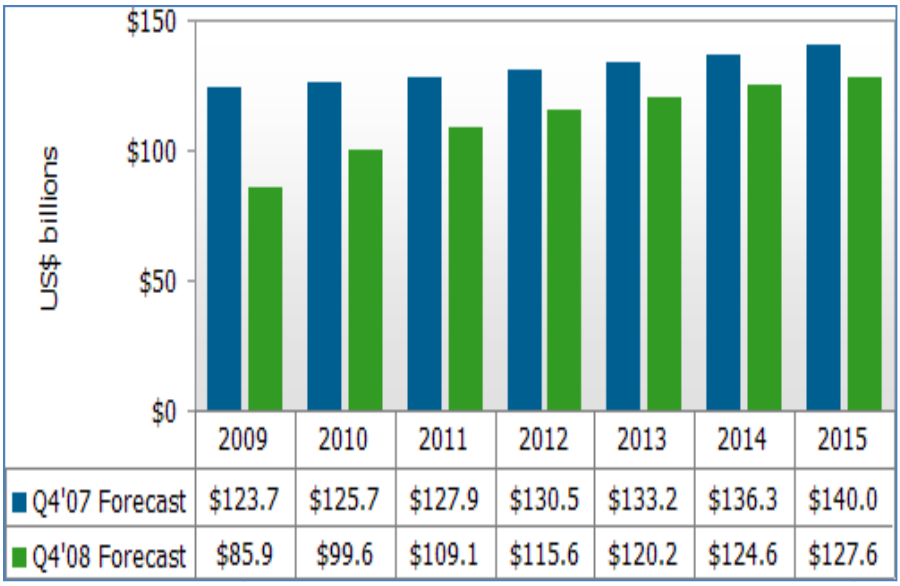

	2009	2010	2011	2012	2013	2014	2015
Q4'07 Forecast	$123.7	$125.7	$127.9	$130.5	$133.2	$136.3	$140.0
Q4'08 Forecast	$85.9	$99.6	$109.1	$115.6	$120.2	$124.6	$127.6

Figure 1.1 2011 quarterly worldwide FPD annual forecast reports [data taken from display search].

Hence there is a huge demand for new materials taking into consideration their potential for the above mentioned applications as well as for accomplishing the goal of increasing conductivity and transparency which depends on a deeper understanding of the structure and electro-optical properties of these materials.

1.2.2 n-type TCOs vs p-type TCOs

The properties of TCOs such as band gap, carrier concentration, and carrier mobilities, arise from the nature of their electronic structures. The n-type oxides are composed of filled d and empty s orbitals. The conduction band is primarily formed by empty metal s orbitals and valence band by filled O 2p orbitals [21]. As an example, Figs. 1.2(a)–(c) illustrate the band structure of ZnO. Conduction band minimum (CBM) is formed by Zn 4s orbitals and valence band maximum (VBM) is formed by O 2p orbitals. These well overlapped wave functions of the

conduction band shown in Figure 1.2 (b) come from the fact that the unoccupied s orbitals of cations have large spatial sizes. Also the small effective masses of these compounds ranging from 0.23-0.35m_e [21] where m_e is the mass of free electron result in high electron mobilities which can reach up to 440 $cm^2/V{\cdot}s$ [22] for ZnO at room temperature, for example. In Table 1.1 we show mobility and carrier density values of few n-type TCOs.

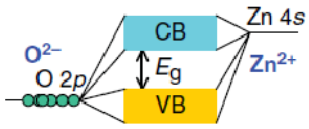

(a)

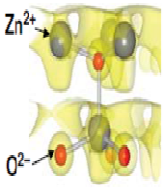

(b)

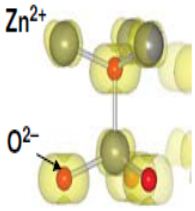

(c)

Figure 1.2 (a) The band structure of ZnO showing that conduction band minimum (CBM) is formed mainly by metal s orbitals and valence band maximum (VBM) is formed by oxygen 2p orbitals. (b) wave functions calculated by density functional theory of the CBM (c) wave functions representing the VBM [21].

However most applications have been limited to passive devices such as sensors, photo catalysts etc. The reason behind very little research has been done in making active devices like p-n junctions might be lack of availability of p-type TCOs. The corresponding p-

type TCOs were not in full realization until Kwazoe et al. [23, 24] discovered a functional p-type TCO thin film, $CuAlO_2$ and opened up a gateway for developing p-n junctions which can generate electricity by absorbing UV/VIS light. Kawazoe et al [23] proposed the chemical design of p-type conducting wide band gap oxides. There is a strong localization of positive holes at the valence band edge of the typical oxide materials due to the ionicity of metallic oxides. Thus the holes are trapped inside as deep acceptors and need high energy to overcome large barrier height to move around in the crystal lattice resulting in poor hole mobility. The possible solution was to introduce a degree of covalency in the metal-oxygen bondings by mixing orbitals of metal cat-ions with O 2p level delocalizing the holes in the valence band edge. This principle was called chemical modulation of valence band (CMVB) and is shown in Figure 1.3.

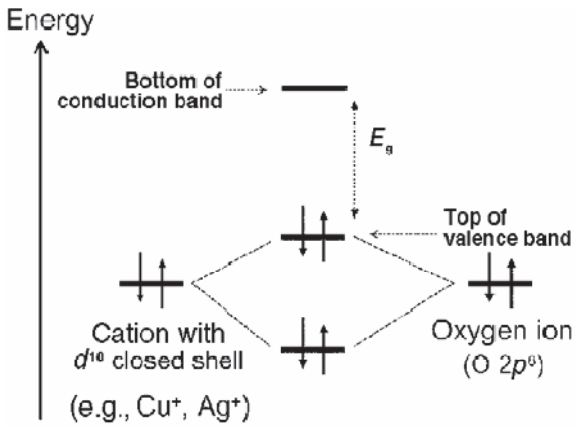

Figure 1.3 Illustration showing the principle of chemical modulation of valence band (CMVB). The top of the valence band consists of cation d and oxygen 2p orbitals. The energy of the closed shell cations are assumed to be the same as that of oxygen 2p electrons [23].

Other examples of p-type TCOs which used doping technique is N-doped ZnO because the activation of the dopants seemed difficult [25]. Yet, the light emitting diodes made of ZnO p-n junction were demonstrated [26]. While the intrinsic ZnO has been mostly used as an n-type TCO, it has been also considered as a candidate for high hole mobility p-type oxide among the

other oxides because the O 2p level is pushed up by the presence of the shallow Zn 3d level, and its dispersion is increased by O 2p – Zn 3d coupling [27].

Other p-ype oxides made of transition metals have been also reported [28, 29] for the fabrication of p-n hetero-junctions [30]. However they often suffer very small built-in-potentials due to very shallow valence band maximum (VBM) very close to conduction band minimum (CBM) of n-type TCOs

The band alignment of several n-type oxides compared with p-type oxides are shown in Figure 1.3 The VBMs of In_2O_3 and SnO_2 are very deep, ~8 eV from the vacuum level (E_{vac}), whereas ZnO has a shallow VBM due to shallow d levels and is a good hole-injection layer. The VBMs of p-type oxides with transition metal elements are more shallow by 2-3 eV than the materials those can be used as an n-type partner in the junction. Nonetheless, the point defect density should be minimized since doping favors acceptor defects in ZnO due to the deep levels as compared to other p-type oxides.

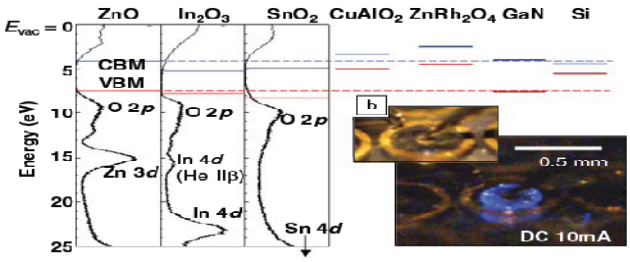

Figure 1.4 The energy band diagram obtained from photoemission spectra shows the valence band maximum (VBM) (red) and the conduction-band minimum (CBM) (blue) of TCOs. Inset (b) shows the blue emission from a ZnO p-n junction LED [21].

1.2.3 Cu-based p-type TCOs

The simplest form of the metal oxide according to CMVB starts with copper oxide. Especially the group of Cu-based p-type TCOs with a delafossite structure and a chemical formula of $CuM^{III}O_2$ where M^{III} is a trivalent cation, have drawn attention, and their examples include $CuAlO_2$, $CuGaO_2$, $CuInO_2$, $CuScO_2$, $CuYO_2$, $CuBO_2$ and $CuCrO_2$.. The small band gap (2.17 eV) of Cu_2O is not sufficient for a TCO material used in visible spectral range [31]. Hence, the band gap is enhanced by alloying Cu_2O with binary trivalent $M^{III}O_2$. These ternary oxides retain the valence band features of Cu_2O with the Cu states dominating the top of the valence bands [24, 32]. The enhancement in the band gap has been attributed to reducing the dimensionality of the Cu-Cu interactions in Cu_2O by alloying with the $M^{III}O_2$. Their crystal structures manifest the argument more clearly. As shown in Figure 1.5 (a), Cu_2O has a simple cubic lattice structure with a space group of O^4_h, Pn3m [33]. Fig. 1.5 (b) shows the delafossite structure of $CuM^{III}O_2$ which belongs to a space group of R3m in which each Cu atom is linearly coordinated with two oxygen atoms with a covalent bond, forming O-Cu-O dumbbells parallel to the c-axis and in turn coordinate to M^{III} atom via ionic force to form $M^{III}O_2$ octahedral units. These layers are stacked alternatively resulting in a hexagonal or a rhombohedral unit cell [34].

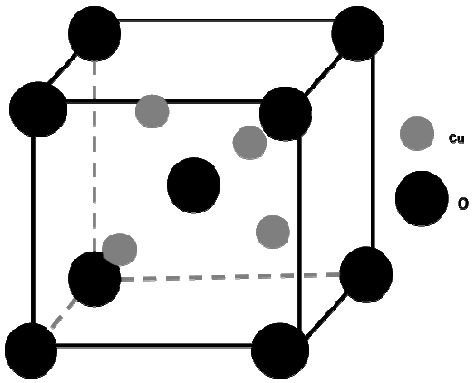

(a)

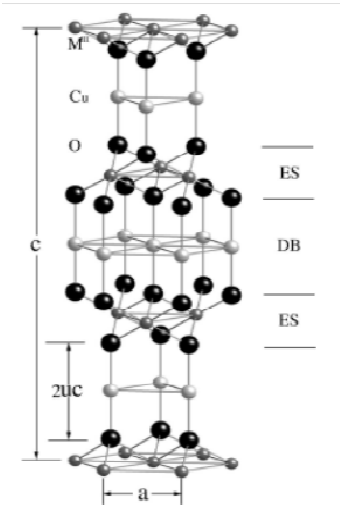

(b)

Figure 1.5 (a) Cubic crystal structure of Cu_2O, grey atoms are Cu and black are O atoms (b) Delafossite crystal structure of $CuM^{III}O_2$, black atoms are O, dark grey and light grey atoms are M^{III} and Cu respectively.

Conductivity studies of $CuAlO_2$ showed a promising value of 17 S/cm corresponding to a hole concentration of 1.2 x 10^{20} cm^{-3} [35, 36]. With the relatively low mobility of $CuAlO_2$ [37], conductivity in delafossites, in general, is primarily limited by hole concentrations. Previous study says the hole contribution in $CuAlO_2$ and other delafossites is mainly determined by Cu vacancies [38]. Nagarajan et al [39, 40] observed increasing conductivity with decreasing ionic

radius of the M^{III} cation, which was explained by the decrease in the bond length between the Cu-O atoms because it leads to better overlap of Cu 3d orbitals with O 2p orbitals resulting in a higher hole mobility. It should be noted, however, that the study does not necessarily predict the higher hole mobility in Cu_2O ($100cm^2V^{-1}s^{-1}$) [41] because its pristine structure is different from that of delafossites and the bond length of Cu-O is longer than delafossites. In fact, the mobility of Cu_2O is expected to be comparable to or higher than that of delafossites due to the presence of potentially facile carrier paths, Cu-O-Cu chains those are missing in $CuM^{III}O_2$ [39]. The covalent interactions between the M^{III} cation and oxygen in Cu-based delafossite TCOs were also discussed [42]. Also, a different study discussed the effect of the M^{III} cation size on Cu-Cu distances which can affect the conductivity as holes transport through Cu atoms [43]. This would probably explain why $CuAlO_2$ intrinsically has a higher conductivity compared to $CuScO_2$ and $CuYO_2$ [43] since the ionic radius of Al is smaller than those of Sc and Y. However the size dependence could not explain why doped conductivity of $CuCrO_2$ is higher than doped $CuAlO_2$.

1.3 Intrinsic defects in Cu-based p-type TCOs and the scope of the thesis research

1.3.1 Chemical identification of defects in Cu_2O

The carrier concentration which is an essential characteristic in determining its electrical conductivities of the TCO materials, strongly depends on the intrinsic defects present and their formation energies. Cu_2O shows intrinsically a p-type conduction and the comparison between the conductivity and capacitance-voltage measurements shows that it is a compensated material i.e., the acceptor concentration is always higher than donor concentration, and the ratio of N_A/N_D in most cases lies between 1 and 10 [7,45-46]. However in Cu_2O, the nature of the intrinsic point acceptors and donors is not completely clear. Both high temperature experiments [46] and ab-initio calculations [1] suggest that the p-type conductivity is due to the presence of Cu vacancies. There are few studies stating n-type Cu_2O could be made using electro-deposition by varying pH of the solution. But theoretically it was proved that Cu_2O cannot be

intrinsically n-type oxide, since the n-type defects the most popular being oxygen vacancy has high defect formation energy (~ 1.2 eV) and deep ionization levels such that they are resonant in the valence band. It was also suggested that the electrodeposited Cu_2O exhibited n-type conduction due to external impurities like Cl [3]. Although there have been several defect characterization techniques including PL [48], deep level transient spectroscopy (DLTS) [49], PALS used to study the intrinsic defects in Cu_2O experimentally, they are indirect in making the chemical identity of the defects. Hence this provided us a motivation to further probe the chemical identity of the nature of defects in Cu_2O using PALS and DBS. PALS conjectured with DBS is used in this study as DBS is an effective method to reveal the chemical nature of the defect that involves in the positron annihilation process. The basic principles of PALS and DBS are discussed elaborately in chapter 2.

1.3.2 Light induced metastable defects in Cu_2O

It has been proposed that the metastable defects observed in the Cu_2O junctions produce time-dependant capacitance, series resistance (R_s), open circuit voltage (V_{oc}) and short circuit current (J_{sc}) can be explained by the mechanism that governs PPC [7,50]. There are several interpretations of PPC effect, out of which the most accepted theory was Kuzel's interpretation of association and disassociation of intrinsic point defects during heating and illumination of the sample [51, 52] - the higher conduction upon illumination is mainly due to the increase in intrinsic acceptor concentration due to mainly disassociation of neutral Cu-Cu complexes. There are several models based on electronic mechanism [53-55] to explain the PPC effect out of which the model of Schick and Trivich [53] proposed that photo-excited electrons are trapped into the donor states decreasing the compensation and increasing conductivity. They used thermally stimulated conductivity experiments to validate their theoretical model. The Strasbourg group [54, 55] advanced the idea into a four donor level electron trap model and introduced a band of recombination centers in the sub-bandgap to explain the PPC spectrum as well as to calculate the decay time constant of the

photoconductivity. All these electronic trap models were disapproved by Biccarri et al [56] since the hole capture rate should be smaller than electron emission rate to have an electron trap, but PPC decay time constants experimentally measured showed that the hole capture cross section is $\ll 10^{-23}$ cm^2, a value uncommonly small compared to the typical hole capture cross section of the charged defects (10^{-15} cm^2) in semiconductors. Also Biccarri claimed they observed a constant ionized donor concentration and an increase in acceptor concentration under like unlike Schick and Trivich's model, which predicted decrease in ionized donor density after illumination. Biccarri further showed, in his transient capacitance measurement on the junction structure under forward and reverse biases, which the time constant for donor filling was much larger than what the trap model would predict. Hence Biccarri et al [56] developed a model based on intrinsic defect complexes *($V_{Cu}^{-} – V_O^{+}$)* to explain their PPC data. However, there has not been any study to directly confirm the defect-based models and their chemical nature. In an attempt to answer relevant questions, we have studied the light induced metastable defects using PALS and DBS if there is any.

1.3.3 Defect formation energies of intrinsic defects in Cu-based TCOs

There have been theoretical intrinsic defect studies of Cu-based delafossite materials using LDA and the studies indicated that the electronic structure of delafossites is important in determining the defect formation energies of the intrinsic defects. For example, Nolan et al [2] investigated the p-type nature of Cu-based delafossites by calculating the formation energies of intrinsic defects and related the dimensionality of Cu-Cu interactions and the proximity of Cu atoms to V_{Cu} formation energy. It was qualitatively explained that the low formation energy in Cu_2O (0.74 eV) compared to $CuAlO_2$ (0.98 eV) was due to the longer bond length of Cu-Cu and more open structure in Cu_2O compared to $CuAlO_2$. Generally, the major acceptor defects in $CuM^{III}O_2$ (M^{III} = Al, In, Y, Sc, and Cr) are copper vacancies due to their low formation energy [57-61], which gives rise to p-type conduction. Though they found other type of defects like oxygen interstitials in $CuAlO_2$, $CuScO_2$, $CuYO_2$ and $CuCrO_2$ and Cu_{In} antisite defects in $CuInO_2$,

which have low formation energies compared to copper vacancies they do not contribute much to conduction due to their deep ionization levels. The values of defect formation energies of copper vacancies along with the ionization levels obtained from several studies have been compiled in Table 1.1. It should be noted that each LDA calculation has a unique set of input parameters used and the care needs to be taken when the data in the table is compared to each other. In order to make a systematic comparison among delafossites with different M^{III} cations and the effect of the cation size on the defect formation energy, the structural and the electronic information of several delafossites are entered into Van Vechten Cavity Model (VVCM) and the defect formation energies of the intrinsic defects are calculated in this study. The principles of VVCM are further discussed in detail in chapter 5.

Table 1.1 Defect formation energies of various Cu-based oxides along with the ionization energies from the literature [57-61].

TCO	**Formation energy of V_{Cu} (eV)**	**Ionization energy of V_{Cu} (eV)**
$CuInO_2$	0.49[61]	0.33[61]
$CuCrO_2$	0.95[60]	0.37[60]
$CuAlO_2$	0.98[2]	0.68[2]

CHAPTER 2

EXPERIMENTAL TECHNIQUES AND MATERIALS

2.1 Experimental Techniques

2.1.1 Positron Annihilation Spectroscopy (PAS)

2.1.1.1 Introduction

It was discovered that the positron can be trapped in the crystal defects, i.e. the wave function of the positron is localized at the defect site until annihilation. Since then, Positron spectroscopy was used first to detect thermal vacancies in metals [62], in ionic crystals [63], and later in semiconductors [64]. The trapping of a positron in defects is based on the formation of an attractive potential at open-volume defects, such as vacancies, vacancy agglomerates, and dislocations. The sensitivity range for the vacancy detection in metals starts at about one vacancy per 10^7 atoms. The positron trapping behavior in semiconductors is more complex compared to metals since positron as a charged particle is sensitive to the charge of the defects. Neutral and negative vacancy-type defects, as well as negative ions are the dominant positron traps in semiconductors. This defines the power of the positron methods in contrast to most electrical and optical spectroscopies.

2.1.1.2 Positron Sources and its Decay Scheme

Positrons can be obtained from the β^+ decay of a radioactive isotope. For example, ^{22}Na decays according to the reaction, $Na^{22} \longrightarrow Ne^{22} + \beta + \nu_e + \gamma$. Na^{22} is the most commonly used positron source due to its several advantages including high positron yield (90.4%) and its easy handling in the laboratories which are sodium salts in aqueous solutions, such as sodium chloride and sodium acetate. The half-life of ^{22}Na is 2.6 years and its cost also makes this a useful positron source. Other radioactive isotopes include ^{64}Cu, ^{58}Co, ^{68}Ge etc. The decay scheme of ^{22}Na is shown in Figure 2.1. 90.4 % of the ^{22}Na source decays by emission of a

positron (β^+) and an electron neutrino to the excited state of ^{22}Ne, and after 3.7ps the ground state of ^{22}Ne is reached by emission of a γ-quantum of 1.274 MeV. The other processes which happen with lower probabilities during this decay with lower probabilities are electron capture (EC) and direct transition to the ^{22}Ne ground state (in Figure 2.1 direct transition is denoted by the left arrow).

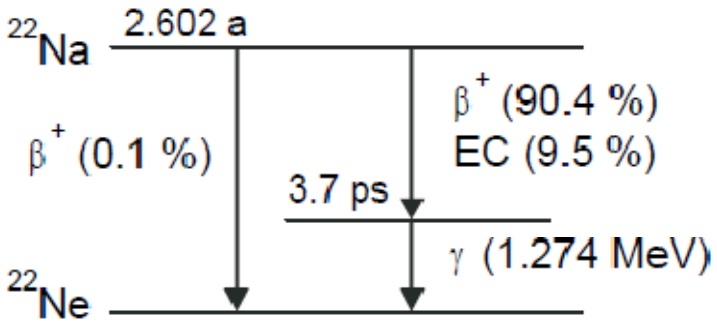

Figure 2.1 Decay scheme of the radioactive isotope, ^{22}Na [65].

2.1.1.3 Principles

Positrons generated from an isotope source (e.g.^{22} Na) first penetrate into the sample, thermalize within a few ps, and diffuse to interact with electrons to be annihilated. The electromagnetic interaction between electrons (e^-) and positron (e^+) makes the annihilation of the e^- - e^+ pair in which the total energy of the annihilating pair is transferred to the quanta of the electromagnetic field, two γ photon, which are emitted in the opposite directions [66]. This reaction can be expressed as the following two photon annihilation process,

$$e^- + e^+ \rightarrow \gamma + \gamma \qquad (2.1)$$

The total energy of the emitted photon is conserved and given by rest mass energy, $E\ (= m_0c^2)$, where m_0 is the rest mass of the electron and c is the velocity of a photon in a vacuum. The above process is characterized by positron annihilation rate, λ ($= 1/\tau$), where τ is the lifetime of the positron. The positron lifetime is registered as the time difference between the emission of the 1.27 MeV γ photon and the 0.511 MeV γ from annihilation. The annihilation rate also depends on the electron density, n_e sampled by the positron. Apart from this, the energy of the

two annihilated photons is shifted by an energy, ΔE (= $\pm cp_z/2$), called the Doppler shift, and also the angle between the emission directions of the two photons is given by $\Delta\theta$ (= $p_{x,y}/m_0c$), where $p_{x,y}$ and p_z denote longitudinal and transverse components of the electron momentum respectively (Figure 2.2). Hence, from PAS, we could estimate λ, and ΔE together with Δθ, using PAS and measuring Doppler shifts of annihilation photon energies plus angular correlation curves respectively. This is schematically explained in Figure 2.2.

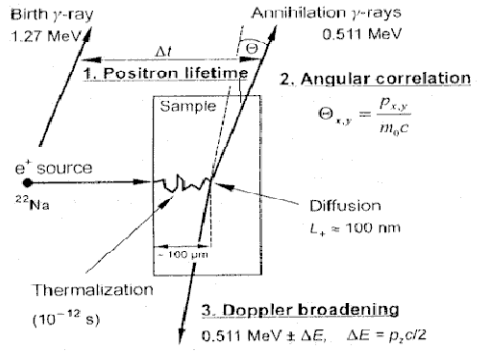

Figure 2.2 Typical scheme of positron experiments [65].

Doppler broadening spectroscopy (DBS) records the shift of energy, ΔE of the 0.511 MeV annihilation line in an energy-dispersive spectrometer. The angular deviation, Δθ of the annihilation quanta is measured from angular correlation of annihilation radiation.

2.1.1.4 Positron Lifetime Measurements

The annihilation of a positron is a random process, and the lifetime spectrum is a statistical distribution which is a representation of characteristic lifetimes of the annihilations occurred in the sample from the time positron was injected into the sample. In a defect free material, the positron decay spectrum is a simple exponential decay whereas the spectrum of a material with defect sites where positrons can be trapped is a superimposition of a number of exponential decays. The experimental setup to measure the positron lifetime is shown in a simple block diagram in Figure 2.3 (a) and the sample and source prepared in a sandwich arrangement is shown in Figure 2.3 (b).

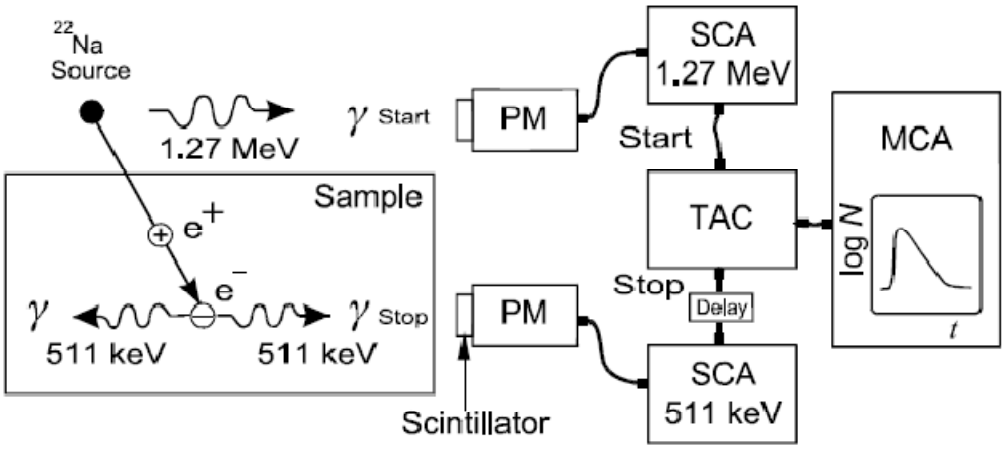

(a)

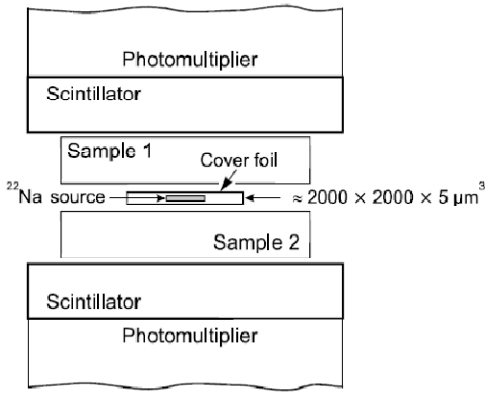

(b)

Figure 2.3 (a) Experimental set-up to measure positron lifetime (b) Sandwich arrangement for sample and a positron source [65].

As shown in the block diagram, the source is sandwiched by two identical samples and the entire arrangement is placed between two scintillator detectors, S1 and S2, coupled to a timed analyser. The detectors are fed through the single channel analysers (SCA) which are tuned for the energy of the two photons and connected to the time-to-amplitude converter (TAC) with a start signal coming from 1.274MeV γ-photon and a stop signal from 0.511MeV γ-photon.

The amplitude of the output pulse is proportional to the time difference between the birth and the annihilation γ-quanta and, thus, represents a measure of the positron lifetime. The single annihilation event is stored after analog-digital conversion in the memory of a multi-channel analyzer (MCA). The channel numbers of the MCA represent the time scale. In this study, more than $5X10^6$ annihilation events were recorded for each lifetime spectrum. The time resolution of the spectrometer was determined by the scintillators and it was about 180 ~ 280 ps. The source and the two identical samples were separated by a thin Kapton foil. In order to ensure the almost complete annihilation of positrons in the specimen volume the foil is placed in between the samples. A minimum sample thickness is required to make sure that the essential fraction of positrons annihilates in the sample pair.

2.1.1.5 Data Analysis

The positron lifetime spectrum is generally the sum of the exponential decay curves given by the following equation,

$$-\frac{dn(t)}{dt} = \sum_i I_i \lambda_i \exp[-\lambda_i t], \qquad \sum_i I_i = 1 \tag{2.2}$$

where *n(t)* is the probability that the positron is alive at time t after its birth and τ_i is the lifetime associated with a decay curve with its initial intensity, I_i. Each lifetime represents the specific type of the defect where positrons are trapped and annihilated as well as the annihilation in the bulk of the material. The number of components to be resolved in the lifetime spectrum depends on the mutual separation of the individual lifetime components their intensity of instrumental resolution, source lifetime, and the statistics. There are several standard computer programs available for the decomposition of the spectra - for example, POSITRONFIT or PATFIT by Kirkegaard et al [67]. For data analysis, background first needs to be subtracted from the spectrum and it is followed by the source correction where the characteristic lifetime spectrum of the source is subtracted, which is generally determined by an individual method. The source components are varied using a single component spectrum of a defect free sample to get a good a good fit. The fitting process continues by varying the parameters for the

component decay curves until the variance of the fit satisfies the minimum requirements. Size and concentration of defects can also be obtained from the lifetime value and its intensity. An example of an experimental lifetime spectrum of Si is shown in Figure 2.4. Two curves of lifetime spectrum are plotted in the Figure 2.4, one for the as grown sample and the other for plastically deformed sample. The curve of the deformed sample is located higher compared to the as-grown indicating the occurrence of long-lived components. After the decomposition of the spectrum the long lifetime components which are related to the defects τ_2 (320ps) and τ_3 (520ps) are found. They are shown as straight lines in the semi logarithmic plot in the Figure 2.4, below. The deviations from the straight lines of higher lifetime components are caused due to annihilations in the source and the background contribution. Always a background subtraction followed by a source correction has to be performed to avoid these kind deviations. The characteristic lifetime spectrum of the source needs to be subtracted from the obtained spectrum of the sample. The determination of the source spectrum is performed by a individual method by analyzing a one-component spectrum of a defect-free sample. Only one lifetime component corresponding to the bulk lifetime τ_b is found which is given by 218ps as shown in the Figure 2.4.

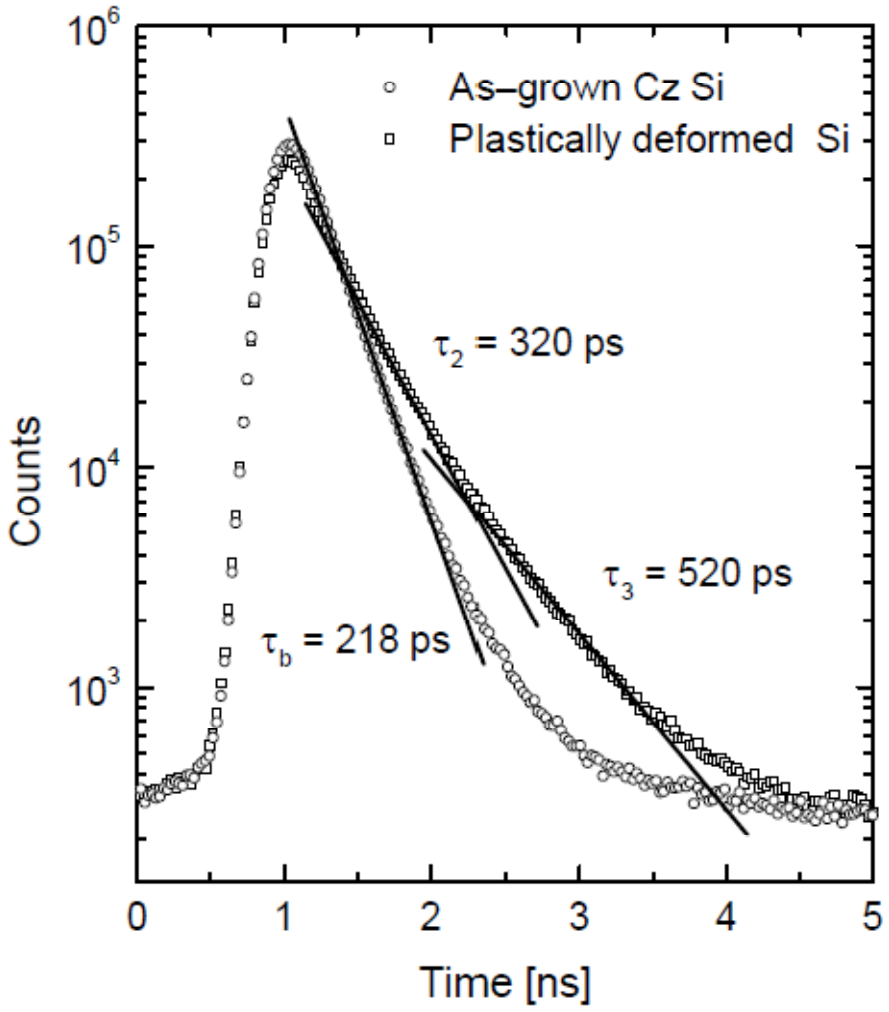

Figure 2.4 Example of a positron lifetime spectrum of as-grown (Czochralski-grown) Si and plastically deformed Si showing a bulk lifetime of 160ps and defect lifetimes of 320 ps and 520 ps [68].

2.1.2 Doppler Broadening Spectroscopy (DBS)

2.1.2.1 Principle and Experimental Set-up

During the annihilation process of the positron, the momentum exchanges between the electron and the positron occurs and it must be conserved into the γ-photon pair. The broadening (ΔE) of the 511 KeV annihilation line occurs due to the Doppler shift in the energy of the annihilating photons and it is equal to $\pm cp_z/2$ where p_z is the longitudinal component of the

momentum of the annihilation pair along the direction of the gamma emission. The momentum of the positron after thermalization in the sample is smaller than that of the electron, which allows to probe the electron distribution around the annihilation site. The effect of localization of the positrons in lattice defects enables us to find out the electron distribution around the open volume defects. When there is a localization of positrons in the open volume defects, the fraction of valence electrons annihilating increases compared with that of core electrons. Also the momentum of the valence electrons gets lower, the momentum distribution of annihilating electrons shifts to smaller values causing smaller Doppler broadening. The major strength of DBS is its sensitivity on the chemical environment of the annihilation site. In fact, the chemical surroundings influence the electron momentum distribution than the electron density.

The experimental setup used for DBS in this study is schematically shown in Figure 2.5. A liquid-nitrogen cooled Ge detector was used as it served as a high resolution energy-dispersive detector system. The source is sandwiched between the sample pair similar to positron lifetime experiments. In our experiments we used one detector as shown in the following figure. The background can be reduced by using a Doppler broadening coincidence technique, which registers both the γ-quanta coming from the two sample pairs. The charge separation occurs of the annihilated photons by an applied high voltage of several kV and is converted by a preamplifier to an electrical pulse. The multi-channel analyzer (MCA) registers the photon energy which is the amplitude of the electronic pulse. The stabilizer which is a part of the MCA allows the long-term collection of several million counts. The time of the measurement of the spectrum is comparable to the positron lifetime spectrum.

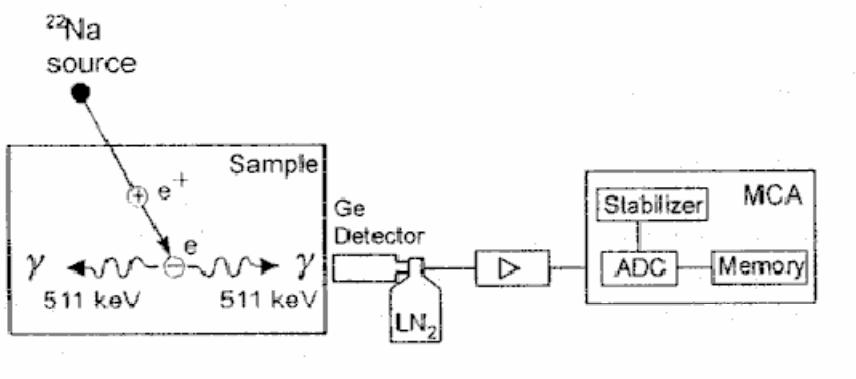

Figure 2.5 Experimental setup for measuring Doppler broadening spectrum [65].

2.1.2.2 Data Analysis

The typical spectrum of DBS is shown in the Figure. 2.6. The spectrum of defect free sample looks broader than that of the defective sample. The DBS spectrum is often characterized by 'S' (shape) and 'W' (wing) parameters and they respectively measure the interaction of the electron-positron pair with the low-momentum valence electrons and high-momentum core electrons. The parameters are calculated respectively as the ratio of the center and the wing area of the spectrum to the entire area of the spectrum. The interval limits are chosen symmetrically around the energy of E_0 = 511 keV for the calculation of the S parameter, $E_0 \pm E_s$. The energy limits to determine W parameter should be chosen in such a way as to have no correlation effects with the S parameter. These chosen limits are kept constant for all spectra to be compared. In the figure 2.6 we could see the limits of 'S' were set to (511±0.8) keV for the determination of S and to (511 + 2.76) and (511 +4) keV for W. are always fixed in order to compare the parameters of different samples. We fix our energy limits of both S and W parameters to about 10 channel widths from the 511 KeV annihilation line.

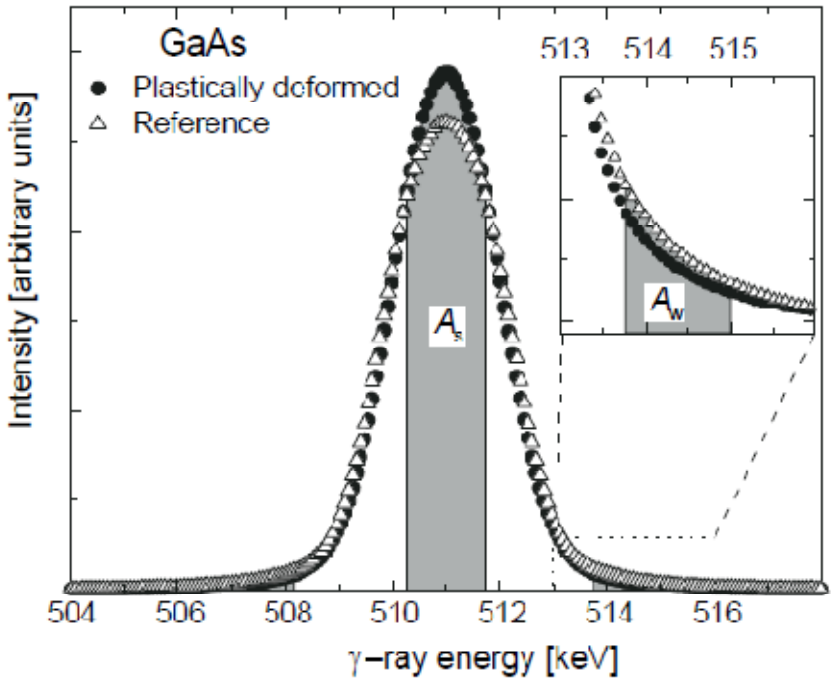

Figure 2.6 DBS spectra from defect-free GaAs sample (triangles) and the plastically deformed GaAs sample (circles). A_s gives the area under the curve close to 511 KeV γ-energy characterizing the low momentum parameter, S and A_w gives the area under the curve away from 511 KeV γ-energy characterizing the high momentum parameter, W [68].

2.2 Materials

PALS and DBS measurements were done on three different samples including Cu_2O powder (Alfa Aesar, 99.9%), CuO powder (Alfa Aesar, 99.9%) and a 1mm-thick disk of Cu (United Copper industries, 99.9%). The powder samples, Cu_2O and CuO were characterized by scanning electron microscopy (SEM) (Hitachi, S-3000N) and X-ray diffraction (XRD) Siemens D-500 powder diffractometer , (PANalytical, X'Pert Pro) to determine the particle size, surface morphology, and the crystal structure. We also performed energy dispersive X-ray spectroscopy (EDS) attached to the SEM (Hitachi, S-3000N) to check the chemical composition of the samples. Additionally, the samples were thermally annealed at 350 ~ 400 ^{o}C under

vacuum prior to any measurement in order to remove any metastable defects remained after their synthesis and fabrication.

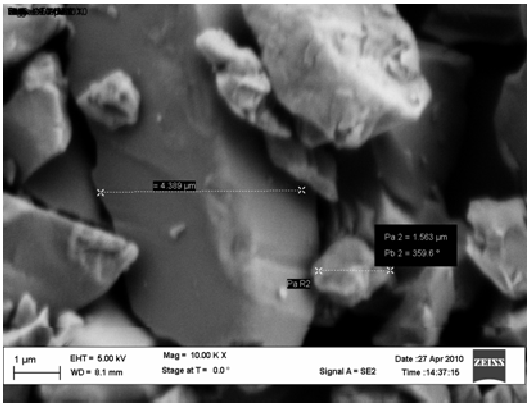

(a)

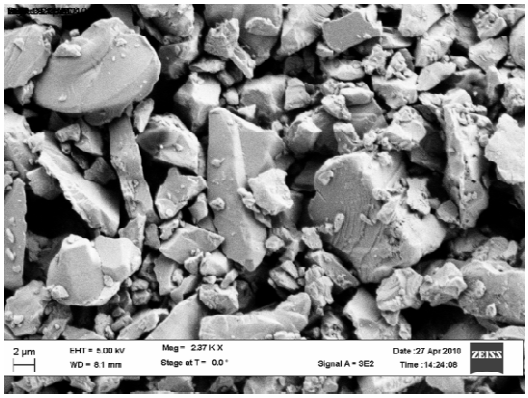

(b)

Figure 2.7(a) SEM image of as-received Cu_2O at 10K magnification (b) SEM image of as-received at 2.37K magnification.

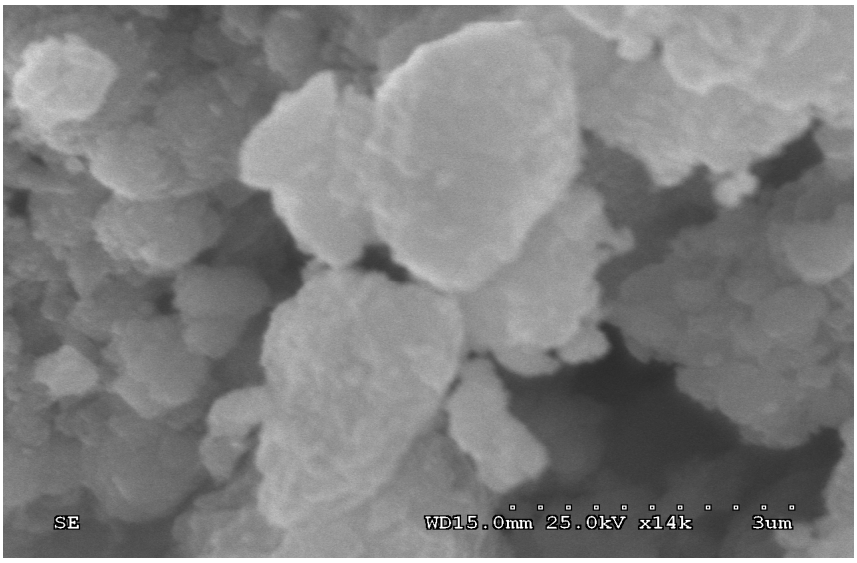

Figure 2.8 SEM image of as-received CuO.

As shown in Figures 2.7 and 2.8, the average particle size of the Cu_2O was over 5 μm, whereas the particle size of CuO was 1 - 3 μm on average. The size of the particle of the powder samples plays an important role in positron spectroscopy experiments. Once the positron enters the sample, it diffuses about 100 nm before annihilation. To avoid the positron penetration into the grain boundaries, the particle size or the grain diameter generally should be larger than the positron diffusion length [69]. Since the particle size was in the order of few μm in this study, there was no probability of the positron being trapping on the surface of the particles. EDS data showed that the compositions of the samples were consistent with the the information provided by the vendors. For example, Table 2.1 showed that the composition of Cu_2O was very close to the stoichiometry of 2 to 1.

Table 2.1 EDS compositional analysis on Cu_2O before annealing.

Element	Atomic%
Cu K	76.24
O K	23.76

The XRD data (Figures 2.11 and 2.12) confirmed the simple cubic structure of Cu_2O with a (111) preferred orientation (PDF# 77–0199) and the tenorite crystal structure of CuO with both (002) and (112) orientations (PDF# 74-1021). Additionally, the phase of Cu_2O remained unchanged after annealing as XRD after annealing did not show any diffraction peak associated with CuO (Figure 2.13).

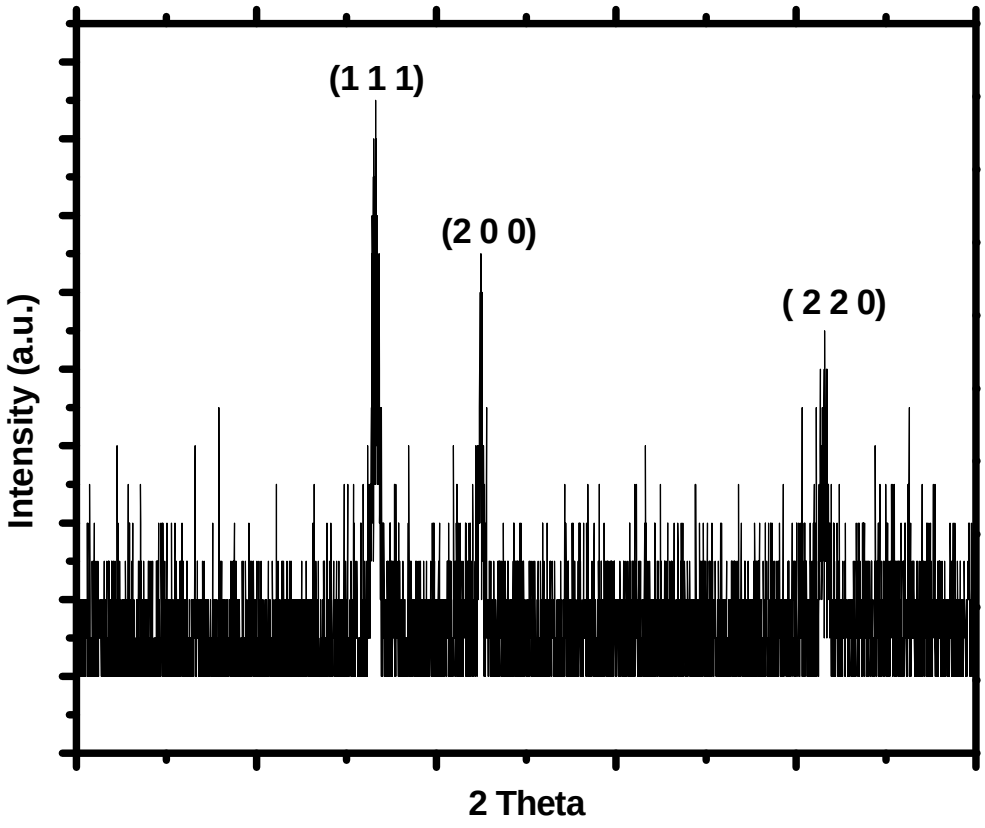

Figure 2.9 XRD of Cu_2O before annealing.

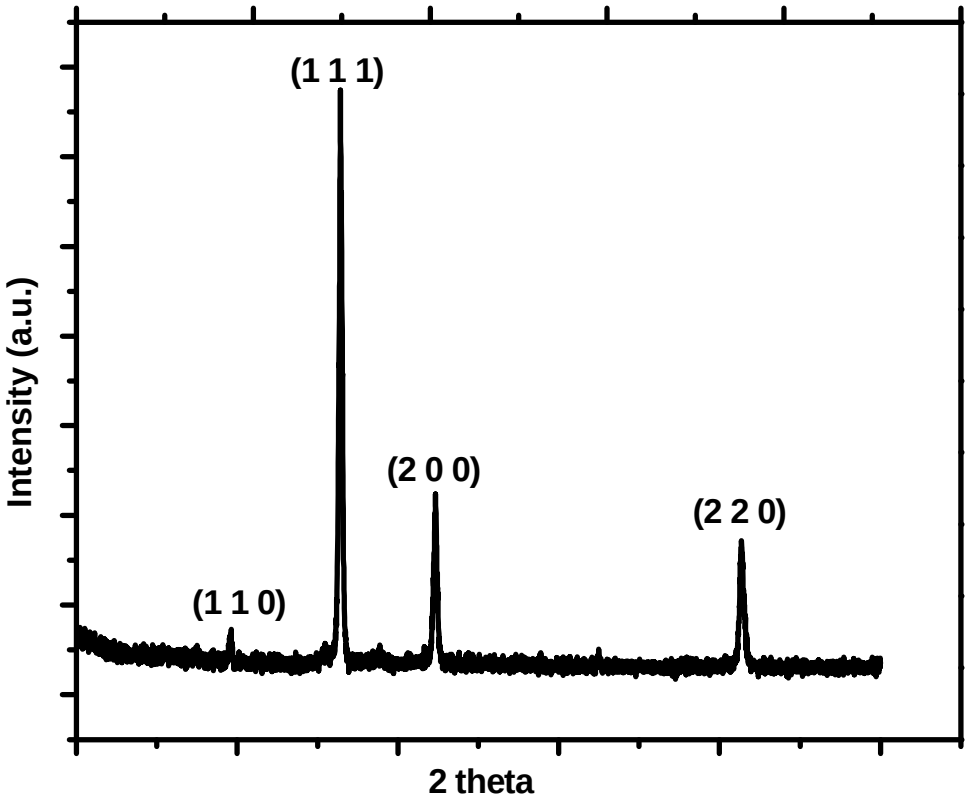

Figure 2.10 XRD of Cu_2O after annealing.

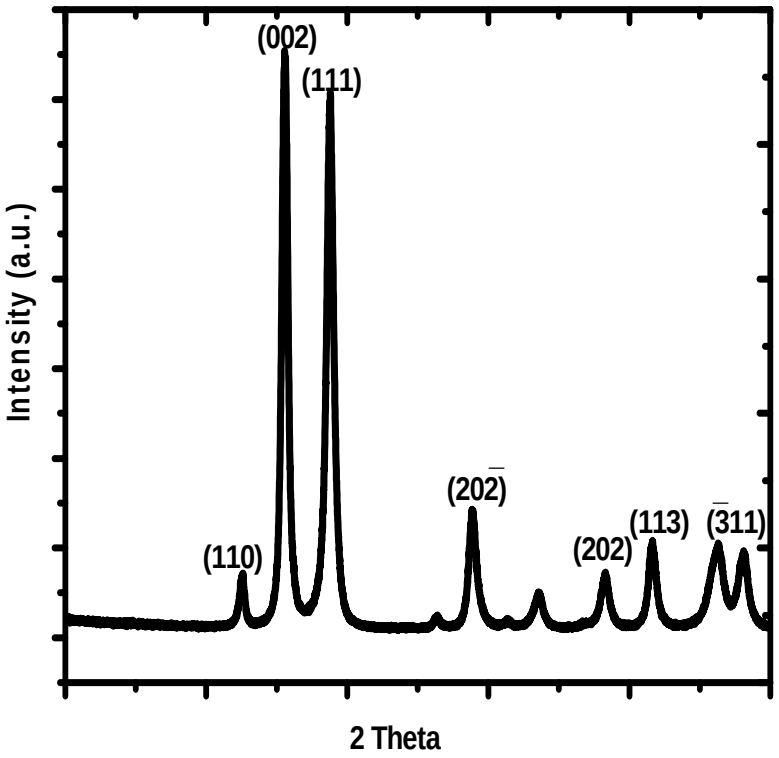

Figure 2.11 XRD of CuO.

CHAPTER 3

POSITRON ANNIHILATION IN COPPER OXIDES AND ITS DOPPLER BROADENING: CONNOTATION OF OXIDIZING Cu AND THE PRESENCE OF Cu VACANCIES

3.1 Introduction

In this study, systematic analysis of positron annihilation in Cu, Cu_2O, and CuO has revealed the common presence of copper vacancies, which is consistent with the change in the formation energy of copper vacancy in the materials. Besides, Doppler broadening of γ-emission from the annihilation showed that the density of low- and high-momentum electrons respectively increases and decreases as the degree of covalency in the material increases. The intrinsic open-volume defects determine the type of majority carriers in semiconducting copper oxides (CuO and Cu_2O), which can be low-cost *p*-type photovoltaic absorbers in semi-transparent solar cells. Using transparent conducting oxides (TCOs) as active photovoltaic junction materials and light absorbers in solar cells is an attractive approach to realize various semi-transparent building-integrated energy-harvesting applications because their large optical band gaps (~2 eV) allow a certain level of transparency in the visible spectrum of natural light. The large band gap, in general, provides a high built-in potential of the junction particularly enabling voltage-driven applications even though the current generated is relatively low. In fact, hetero-junctions between *p*-type Cu_2O and *n*-type ZnO-based TCOs have achieved a power conversion efficiency up to 4.04% [70, 71]. Finding device-quality *p*-type TCOs, however, has been challenging because the hole mobility in metal oxides is generally low due to the lack of covalency in their valence bands. Cu-based oxides are often exceptional because having energy level of the fully filled *d* orbital of the copper close to the 2*p* orbital of oxygen allows

sizeable covalency in their bonds forming a substantially delocalized valence band edge [23]. Intrinsic form of Cu_2O, for example, has a bandgap of about 2.17 eV [31], often shows *p*-type electronic conduction [7, 46].

In this work, positron annihilation lifetime spectroscopy (PALS) in conjunction with Doppler broadening spectroscopy (DBS) and photoluminescence (PL) spectroscopy was performed on pure Cu and copper oxides in order to understand the electronic alteration made on Cu by its oxidation and its implication in the electronic environment of vacancies in copper oxides.

3.2 Experiments

PALS and DBS measurements were done on three different samples including Cu_2O powder (Alfa Aesar, 99.9%), CuO powder (Alfa Aesar, 99.9%) and a 1mm-thick disk of Cu (United Copper industries, 99.9%). Each sample was mounted in a plastic container for the PALS and DBS measurements. ^{22}Na and ^{68}Ge were used as a positron source respectively for PALS and DBS and the activity of the source was 7.5 μCi and 1.7 μCi correspondingly. The source was covered by thin Kapton foil and sandwiched by two identical samples. Two units of photomultiplier tube with a BaF_2 γ-scintillator (Photonics, xpq2020) and a high-purity(HP) Ge coaxial γ-detector (Canberra 2020) were used for PALS and DBS respectively and ORTEC electronics include a multi-channel analyzer and a time-to-amplitude converter. The LT spectrometer setup if a fast-fast system using EEG model 583 Constant Fraction Discriminators (CFDs) and an EGG Time to Analog Converter (TAC) model 566. The resolution of the lifetime spectrometer used and the HP-Ge detector ranges about 400-450ps and 1.3KeV respectively. The number of counts for each PALS spectrum was about 10^6 and the data was analyzed using an analysis software (LT, version 9) [72]. The lifetime spectra analyzed after subtracting the background and the source corrections were deconvoluted into Gaussian resolution functions with their characteristics lifetimes. For the deconvolution process, the lifetime associated with the annihilation in the bulk of material was fixed according to the literature value and the number

of lifetimes was specified by users. The S and W parameters from DBS are determined respectively from the energy range of 511 ± 1 keV and 508 ± 1/514 ± 1 keV. The PL measurements were performed at room temperature using an Ar laser with an excitation wavelength of 532 nm.

3.3 Results and Discussion

The annihilation parameters for all the samples are compiled in Table 3.1 The bulk lifetime of 121 ps was fixed for pure Cu according to the reported lifetime value [73, 74]. While the lifetime of 165 ps was also identified in the disk of Cu and assigned to V_{Cu}, relatively high formation energy of V_{Cu} (1.13 ~ 1.28 eV) in pure Cu [75] and its consequently low population explain very small contribution of V_{Cu} (~ 2%) in positron annihilation. Although the experimentally determined lifetime associated with V_{Cu} was rarely reported, the set of lifetimes obtain from Cu is quite consistent with previous studies [73-74, 76]. Unlike the pure Cu, copper oxides showed clear presence of open-volume defects in the positron annihilation. Two characteristic lifetimes (230 ps and 358 ps) were found in the Cu_2O with the fixed bulk lifetime of 171 ps [5]. The lifetime of 230 ps is first assigned to V_{Cu} as their dominant presence is expected from its low formation energy (< ~ 0.7 eV) [1]. The longer lifetime of 358 ps is attributed to the clusters of V_{Cu} because defects with a larger open-volume have a lower electron density and it takes longer time for positrons to annihilate. While the presence of complexes between Cu and O vacancies as another type of large open-volume defects in Cu_2O is possible, it is less likely to be the origin of the longer lifetime because their formation energy is generally much higher than that of V_{Cu} - 4.58 eV for $2V_{Cu}+V_O$ complex, for example [77], and the stable charge state of the complex has been estimated to be positive, from which the positron is expected to have a relatively low probability of annihilation at the complex. The lifetimes from pure Cu are generally shorter than those from copper oxides because metallic Cu has a large coulomb screening from the dense population of free electrons. Overall, 30 ~ 40% of the γ - radiation was from the annihilation at defects. For the CuO sample, the bulk lifetime of

169 ps was fixed according to a previous PALS study [6] and two lifetimes of 230 ps and 469 ps were also identified and assigned respectively to V_{Cu} and the clusters of V_{Cu} due to the lowest formation energy of V_{Cu} (< ~ 0.5 eV) among other defects in CuO [78]. The lower formation energy of V_{Cu} in CuO compared to Cu_2O can explain the longer lifetime of the vacancy cluster in CuO because the bigger size of cluster can be expected from the higher population of V_{Cu} in CuO. Higher defect density also explains its relatively large contribution (~66 %) in positron annihilation.

Table 3.1 Positron annihilation parameters, the defect and the bulk LT values and the S, W parameters for copper disk and copper oxide samples.

Sample	**Lifetime (ps)**	**Contribution (%)**	**Defect assigned**	**S**	**W**
Cu disk	121	98.1	bulk	0.4837	0.0474
	176 (±12)	1.9	V_{Cu}		
Cu_2O	171	68	bulk	0.5168	0.0358
	230 (±24)	22.1	V_{Cu}		
	358 (±21)	9.9	V_{Cu} clusters		
CuO	169	34.1	bulk	0.5260	0.0287
	230 (±15)	40.0	V_{Cu}		
	469 (±31)	25.9	V_{Cu} clusters		

The data from DBS provides further insight on V_{Cu} and also difference in the electronic structure between Cu and copper oxides in general. While the S and W parameters are rather similar among copper oxides, the pure Cu shows comparably lower S and higher W (Table 3.1). One possible explanation can come from the difference in the chemical nature of the vacancies in copper oxides and the pure Cu. Since V_{Cu} in pure Cu with a face-centered cubic crystal structure must have Cu atoms as its neighboring atoms, the difference between copper oxides and Cu can be explained only by the presence of V_{Cu} coordinated by oxygen atoms. Assuming the electron momentum distribution in the bulk of Cu and the vicinity of V_{Cu} in Cu is similar because Cu is a mono atomic metal, the S and W parameters purely from the positron annihilation at V_{Cu} could be similar with those of bulk annihilation. The nature of the ionic

bonding component between Cu and O can easily support the premise of V_{Cu} surrounded by oxygen atoms. Cu_2O has a simple cubic crystal structure [33] and a Cu atom is coordinated with two nearest-neighboring O atoms while four Cu atoms surround one O atom tetrahedrally. Monoclinic CuO also shows that Cu and O atoms are coordinated by each other and a Cu atom is neighboring with 4 O atoms in an approximately square planar configuration [79]. The presence of V_{Cu} was further complemented by room-temperature PL measurement of Cu_2O (Fig. 3.1) showing a luminescence peak at 965 nm. The PL signature can be assigned to V_{Cu} according to the previous PL study performed with Cu_2O synthesized under high oxygen pressure to promote the high concentration of copper vacancies [80].

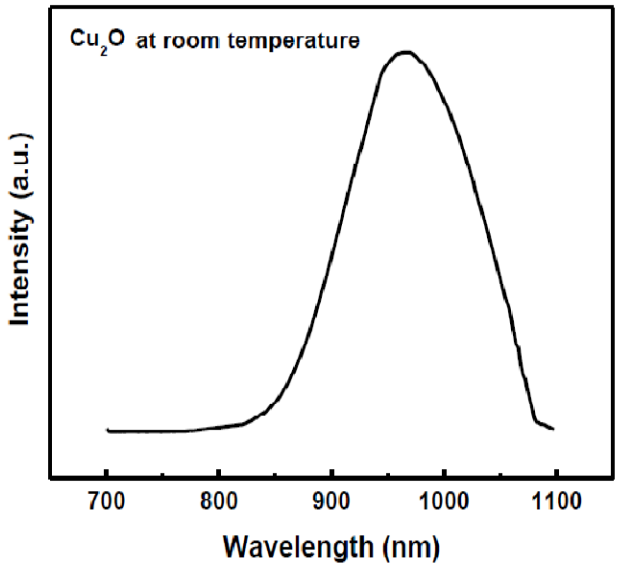

Figure 3.1 Room Temperature PL measurements of Cu_2O.

Further discussion is possible from the set of S and W data plotted in the S-W plane, which shows a linear trajectory between S and W (Fig. 3.2). As often appeared in DBS studies in the literature [81, 82], the linearity can be explained by the change in the concentration of the identical defect in the series samples and it supports the presence V_{Cu} as both S and W vary almost linearly with the concentration of V_{Cu}. However, care must be taken in the analysis because S and W also include the contribution from the annihilation in the bulk of materials. As

a matter of fact, a higher density of core electrons in the pure Cu than oxides can explain its relatively higher W and lower S compared to those of oxides. Since the annihilation is from either bulk of material or defects, it is not surprising that the S and W also linearly scale with the amount of the contribution from the bulk annihilation. Consequently, the difficulty of analysis lies in the fact that increasing the level of oxidation from pure Cu to CuO via Cu_2O increases both the concentration of V_{Cu} and the content of oxygen in the bulk of materials and the resulting change in S and W can be explained by either of them or both.

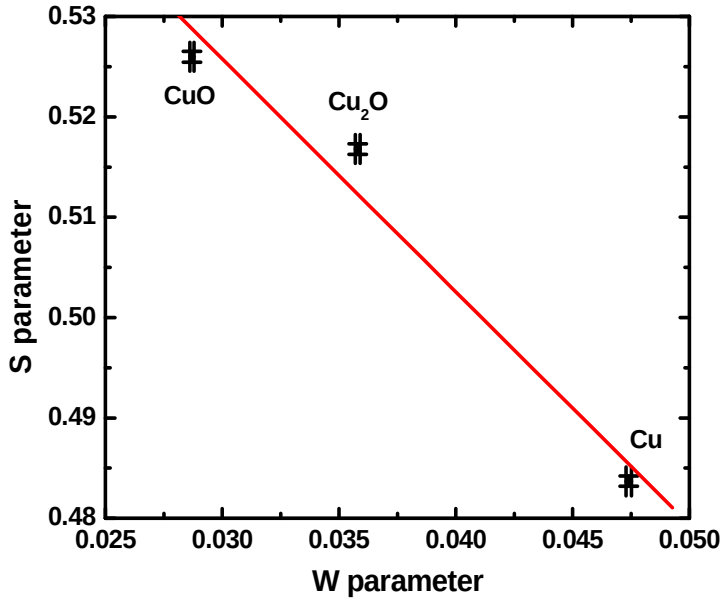

Figure 3.2 S-W plot of the Cu_2O, CuO and Cu disk.

The overall difference in the momentum density of electrons relevant to the positron annihilation in Cu and copper oxides is conjectured through Figure 3.3. The normalized DBS spectra clearly show the difference between pure Cu and copper oxides (Figure 3.3(a)). Because the standard DBS such as what was performed in this study has high intensity of background in W region [83], the focus of the analysis is made on the S region. The ratio between normalized spectra of pure Cu and copper oxides (Figure 3.3(b)) has clearly showed that the density of low momentum valence electrons (up to 10^{-2} m_0c) increases proportionally with the level of oxidation, while the contribution from higher momentum core electrons changes

in an opposite way. Deeper understanding of the change in the momentum density of electrons can be sought theoretically and a previous study on Fe_3O_4 confirmed that the even weak covalency between Fe 3*d* and O 2*p* states can tremendously modify the momentum distribution [84]. Intuitively, the increase in the degree of covalency is expected to modify the momentum distribution at V_{Cu}-related defects as well as in the bulk of copper oxides in the same context and deconvoluting the entire DBS data into each contribution from bulk and defects remains to be studied. Intuitively, the increase in the degree of covalency is expected to modify the momentum distribution at V_{Cu}-related defects as well as in the bulk of copper oxides in the same context and deconvoluting the entire DBS data into each contribution from bulk and defects remains to be studied.

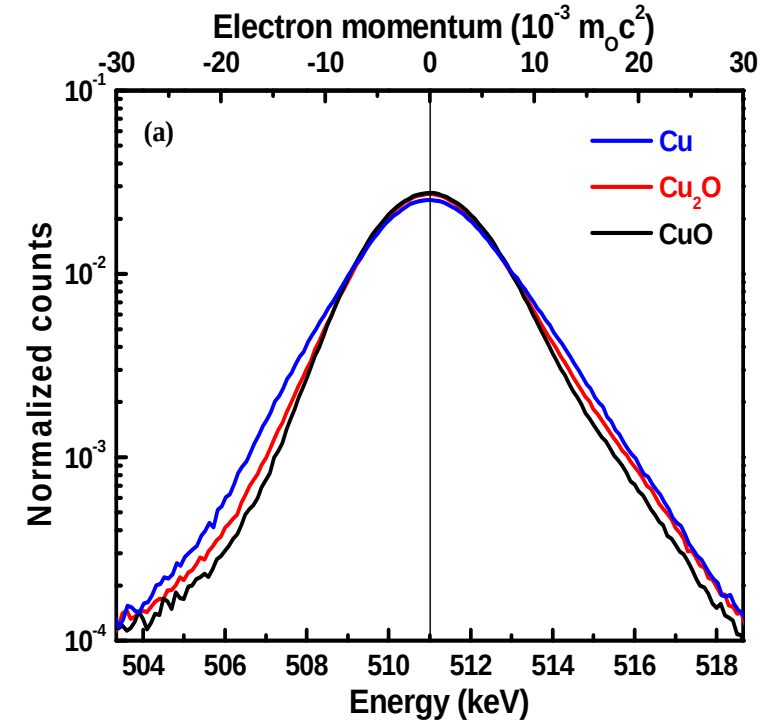

(a)

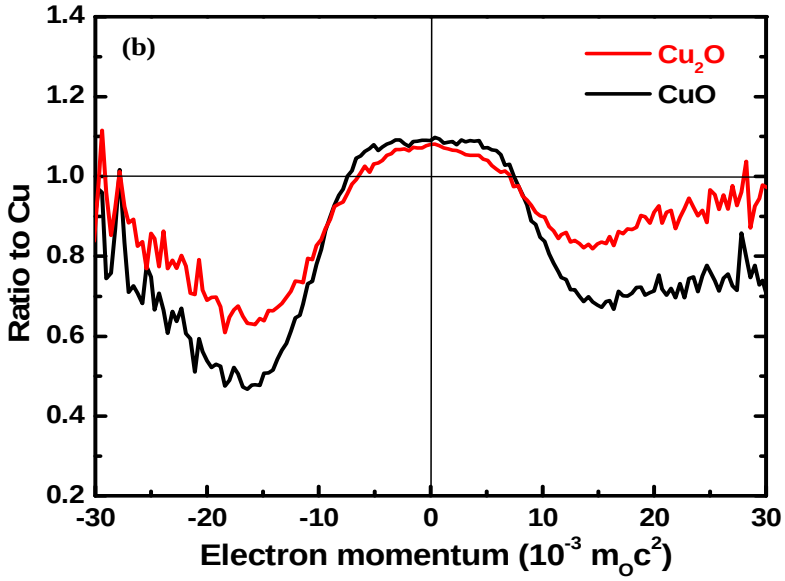

(b)

Figure 3.3 (a) Normalized DBS spectra of Cu, Cu_2O, and CuO
(b) Ratio of the Normalized spectra of copper oxides to pure Cu.

3.4 Summary

In conclusion, the characteristic lifetimes of V_{Cu} and its clusters in positron annihilation were identified and the presence of V_{Cu} was further supported by the analysis of Doppler broadening and photoluminescence measurement. The change in the momentum distribution of electrons participating in the positron annihilation was systematically explained by the degree of hybridization between Cu 3*d* and O 2*p* states. It is likely that the hybridization makes similar impact on momentum distribution at both bulk and defects and it would be difficult to use it as a basis for deconvoluting the entire annihilation into each contribution.

CHAPTER 4

LIGHT- INDUCED METASTABLE DEFECTS IN Cu_2O STUDIED BY POSITRON ANNIHILATION SPECTROSCOPY

4.1 Introduction

As introduced briefly in chapter 1 (Sections 1.1 and 1.3.2), PPC effect in (Cu_2O) has been reported by several groups and explained by different electronic models [50-56]. PPC effect describes an increase in the conductivity of Cu_2O upon light illumination and its extremely slow decay in dark at room temperature. The equilibrium state of the conductivity can be quickly re-established by heating the sample at an elevated temperature as the process turned out to be thermally-activated. From the explanation of the electronic model [53] the increase in conductivity was attributed to increase in acceptor concentration in Cu_2O. Due to the PPC effect a metastable defects influence the junction characteristics of Cu_2O/ZnO solar cells including open circuit voltage, short circuit current, and series resistance [7, 50].

Although the identity of the metastable defects is very important, there has been no definitive experimental study, which clarified the origin of these metastable defects till date. In this part of study, the effect of light illumination on the defect complexes in Cu_2O has been investigated using positron annihilation lifetime time spectroscopy (PALS). Because the positron lifetime is sensitive to the type of defects, the presence of the light-induced metastable defects was expected to be reflected by the change in the lifetime of positron.

As mentioned in the section 1.3.2, two interpretations exist to explain the PPC effect - Kuzel's theory and electron mechanism. Kuzel's theory proposes that the association and dissociation of the intrinsic point defects occurs during heating and illumination processes respectively. Electron mechanism explains PPC effect as the phenomena in which electrons are trapped in deep centers and then re-emitted slowly with time. These theories are explained in detail in the following section.

4.2 Background

4.2.1 Defect complex model

Kuzel et al [51, 52] supposed that both single Cu vacancies and complexes formed by two Cu vacancies are acceptors. At equilibrium, most of the Cu vacancies are coupled with each other to form complexes in the dark. Illuminating the sample dissociates the complex and each complex gives rise to two copper vacancies, thus increasing the acceptor concentration to twice its original number. This can be described as follows.

$$V_{Cu}^{0} + V_{Cu}^{0} \underset{\text{Illumination}}{\overset{\text{heat}}{\rightleftharpoons}} (V_{Cu} + V_{Cu})^{0} \quad (1)$$

When oxygen vacancies (V_O) are present as donors, several other possible complexes can exist as follows [9, 85].

$$V_{Cu}^{-} + V_{O}^{+} \underset{\text{Illumination}}{\overset{\text{heat}}{\rightleftharpoons}} V_{Cu}^{-} - V_{O}^{+} \quad (2)$$

$$V_{Cu}^{0} + (V_{Cu}^{-} - V_{O}^{+}) \underset{\text{Illumination}}{\overset{\text{heat}}{\rightleftharpoons}} V_{Cu}^{0} - (V_{Cu}^{-} - V_{O}^{+}) \quad (3)$$

From scheme (2), the association makes one acceptor (V_{Cu}) and one donor (V_O) dissappear and N_A–N_D (the total acceptor concentration and donor concentration) remains constant. According to Kuzel's [51, 52] experiments scheme (2) was not possible since there was a increase in the conductivity when the sample was illuminated and it decreased when the same sample was heated at a temperature of 150°C. According to the above explanation if N_A-N_D has to remain constant, then they should observe an increase in conductivity, then with illumination there should be association of the defects and during heating they should dissociate, which is contradictory to the observations. Also the calculations of their pre-exponential factors of their samples did not agree with the pre-exponential factors for the

sample having high concentration of donors formed by oxygen and hence ruled out scheme (2). The complexes described by scheme (3) are also possible and they are analogical to the complexes of color centers in ionic crystals. During the cooling process of the sample the concentration of V^{-}_{Cu} and V^{+}_{O} will be reduced by the formation of neutral pairs ($V^{-}_{Cu}\ V^{+}_{O}$) [85]. In conclusion from the Kuzel's work when Cu_2O is illuminated dissociation occurs mainly due to scheme(1). According to Bloem's work there is a possibility of all the three schemes. While the above mentioned results are possible explanations to explain the PPC effect, the electronic models [53,9,55] explain this phenomenon based on a changed concentration of un-ionized acceptors due to preillumination.

4.2.2 Electronic models

This section presents a detailed introduction of the electronic models to explain the PPC effect in Cu_2O. Trapping mechanism was first introduced by Schick et al [53]. Illumination causes the transfer of electrons from the ionized acceptors states into the trapping states or the donor states and hence increases in the conductivity by increasing the ratio between the number of acceptors to the number of donors. This effect persists after the illumination if the donor level is deep enough because the trapped electrons will be emitted after a long time. To calculate the energy levels associated with the defect levels in their model, they performed thermally stimulated conductivity (TSC) experiments. They measured conductivity with the illumination at low temperatures and then in the dark increased the temperature at a constant rate. The peaks which emerged in the TSC curve were due to the thermal emission of the electron from the donor levels and the temperatures at which these peaks occurred denoted the trap depths that represent the position of the defect levels (donor levels) in the band gap. The proposed energy level diagram of Cu_2O according to the results from the experiments (TSC curves) is shown in Figure 4.1 and it consists of two donor levels - 1.03eV and 1.34eV below the conduction band – those were assigned to different charge states of oxygen vacancy. Meanwhile, the acceptor level located at 0.4 eV above the valence band was assigned to Cu

vacancy. They referred to Bloem's work to assign the defect levels as oxygen and copper vacancy levels. To calculate the energy difference between the trap levels and top of the valence band, they measured excess conductivity as a function of photon energy. The energy at which the excess conductivity became zero was the energy difference between the trap level and the top of the valence band and they were 1.1 eV and 1.3 eV as shown in Figure 4.1. The results were, however, inconsistent with to their hypothesis because the sum of the donor level with respect to the conduction band edge and the corresponding energy level found by excess conductivity measurements was not equal to the band gap of Cu_2O. The sum was found to be 2.33 eV for one trap level and 2.44 eV for another and either of them was slightly greater than Cu_2O band gap which is 2.1eV. Apart from this there was no experimental evidence to identify the defect levels except their results were based on Bloem's work. This model is inadequate in explaining the PPC effect and, hence more elaborate models were needed.

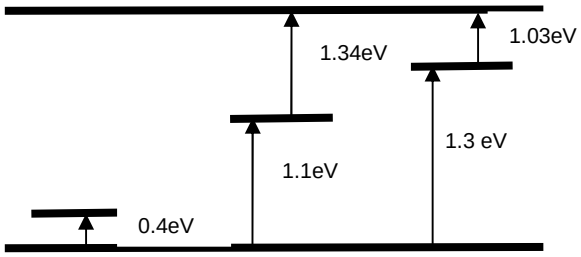

Figure 4.1 Proposed energy level diagram for Cu_2O. The lowest level is an acceptor level and the two higher levels are trap levels [53].

A similar model proposed by Strasbourg et al [9,55] to explain PPC included four donor levels (two shallow and two deep levels) and a band of recombination centers extending from 0.45 eV to 0.65 eV from the valence band as shown in Figure 4.2. The chemical nature of these trap levels was not studied.

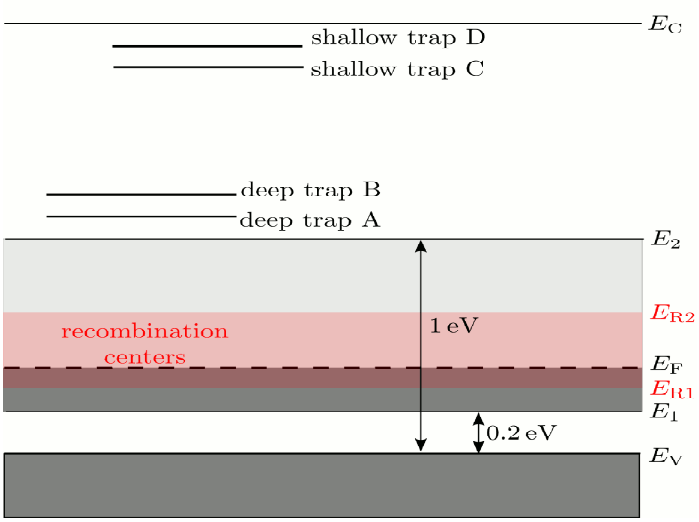

Figure 4.2. Electronic model proposed by Strasbourg group.

Biccari et al [54,56] disapproved any of the electronic models because, to have an electron trap, the hole capture rate should be smaller than the electron emission rate. However, their experiments and calculation showed that the hole capture cross section was << 10^{-23} cm^2, which is uncommonly small compared to the cross section seen in typical semiconductors (~10^{-15} cm^2).

4.2.3 Acceptor-Donor complex model to explain PPC effects

From the above sections, we have seen that the electronic models could not explain some of the experimental results. They were based on one or more electronic levels which can only emit or capture carriers. Biccari et al [54, 56] developed a defect complex model based on a mechanism analogous to that involved in the dynamics of iron-boron complexes in silicon to explain the PPC effect in Cu_2O. To calculate the defect concentration, conductivity vs. temperature experiments have been performed on two samples - one equilibrated (kept in the dark until the conductivity reached minimum) and the other pre-illuminated (illuminated with white light until the conductivity reached maximum). The results (Figure 4.3) and it shows that the hole concentration of the pre-illuminated sample was about 3~7 times higher than the equilibrated sample throughout the entire temperature range.

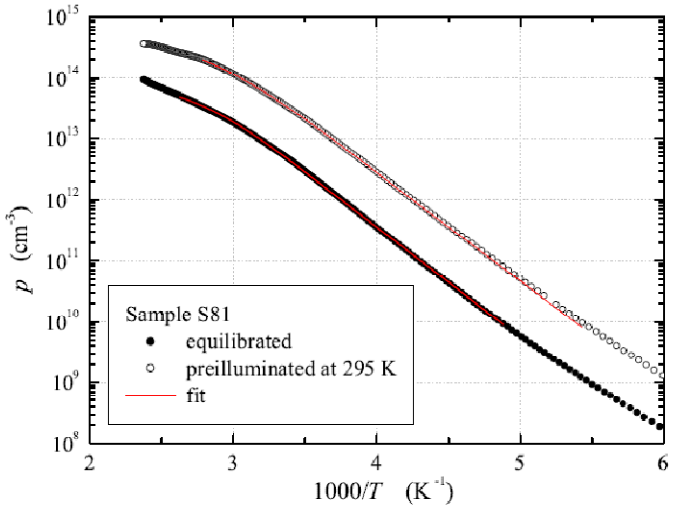

Figure 4.3 Hole concentration as a function of temperature [56].

The experimental data was fitted with (4.1), which is valid for any p-type semiconductor, to obtain acceptor concentration, N_A, ionized donor concentration, N_D^+, and acceptor energy level, E_A.

$$p(T) = -\frac{1}{2}\left(\frac{N_V}{e^{E_A/kT}} + N_D^+\right) + \frac{1}{2}\sqrt{\left(\frac{N_V}{e^{E_A/kT}} + N_D^+\right)^2 + \frac{4N_V N_A}{e^{E_A/kT}}} \quad (4.1)$$

where N_v is the effective density of states of the valence band and it is equal to $2.13 \times 10^{15}\, T^{3/2}$ cm^{-3}. k is the Boltzmann constant and the values of N_A, N_D^+, E_A, and the compensation ratio of N_A/N_D^+ from the fit are shown in Table 4.1. The above expression holds only if N_D^+ is constant during the measurements, and this assumption was validated since the donor levels are deep in Cu_2O and do not contribute towards the donor concentration. From Table 4.1, it is seen for the preilluminated case the acceptor concentration is twice of the equilibrated case.

Table 4.1 Acceptor concentration, N_A, ionized donor concentration, N_D^+, and acceptor energy level, E_A obtained from the fit of p(T) using equation 4.1 [56].

state	N_A (cm^{-3})	N_D (cm^{-3})	E_A (eV)	N_A/N_{D+}
equilibrated	5.72×10^{14}	4.91×10^{14}	0.325	1.16
preilluminated	10.30×10^{14}	4.94×10^{14}	0.322	2.07

Other set of experiments were performed to measure PPC decay time constants. Samples were illuminated until the photo-conductivity reached their maximum and the conductivity was monitored under the dark at three different temperatures. The results are shown in Figure 4.4.

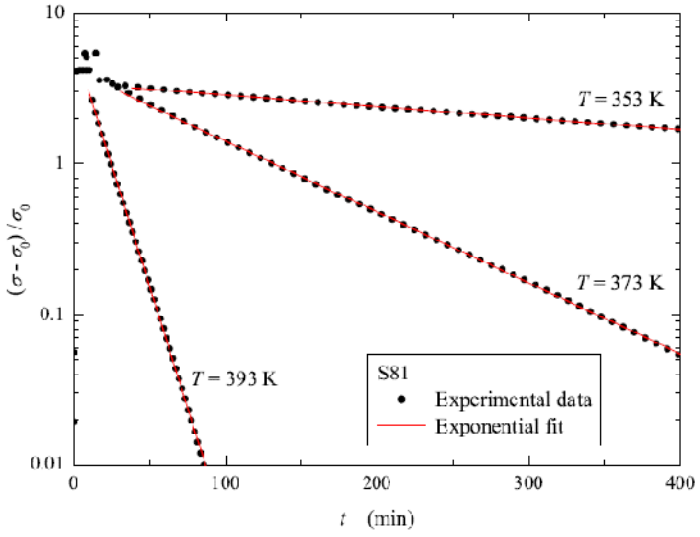

Figure 4.4 PPC decay of Cu_2O under the dark as a function of time at three different temperatures [56].

After the light was switched off, the conductivity decayed exponentially. The conductivity decayed much faster at higher temperature (393K) compared to low temperature (353K). The data was fitted by an exponential fit and is denoted by a red straight line as shown in Figure 4.4. The PPC was monitored as a change with respect to dark conductivity, σ_0. The PPC decay constants were plotted according to Arrhenius plot as a function of temperature which showed an activated behavior and fitted by the following equation.

$$\tau_{PPC} = \tau_0 e^{E_{PPC}/(kT)} \quad (4.2)$$

where τ_{PPC} is the decay time constant, τ_0 is a constant, and E_{PPC} is the activation energy calculated from the fit. The decay time constant at three different temperatures and the values obtained from the exponential fit are shown in Table 4.2.

Table 4.2 PPC decay times for three samples at different temperatures.

sample	τ_{PPC}(353 K) (s)	τ_{PPC}(373 K) (s)	τ_{PPC}(393 K) (s)	E_{PPC} (eV)	τ_0 (s)
S81	784	5132	35110	1.13	2.22×10^{-12}

To explain the results from the experiments, a defect complex model was introduced. The model was based on the effect of electrostatic interaction between the defects on their electronic levels in the band gap. The defect complex (V_{Cu} - V_O) denoted by W was formed by pairing a donor (V_O) with an acceptor (V_{Cu}). In this model, it was assumed that the acceptor is Cu vacancy and the donor is oxygen vacancy. This complex, W can exist in four possible charge states ++, +, 0, and -. The two stable configurations are W^+ and W^0 assuming the interaction is mainly electrostatic. From the temperature range of the above experiments, the complex W^+ is always stable and W^0 dissociates spontaneously. The binding energies of 0.84 eV and 0.42 eV correspondingly for W^+ and W^0 were calculated assuming the donor-acceptor distance of 0.48nm. Figure 4.5 shows a proposed diagram of the energy levels. V_{Cu}^- as the acceptor level is known to be approximately at 0.3 eV from the top of the valence band and the other two electronic levels are $V_O^{++/+}$ and $V_O^{+/0}$ associated with the isolated oxygen vacancy with a positive correlation energy, U by assuming the isolated metastable oxygen vacancy is V_O^+ and the equilibrated state is the doubly charged positive state. The complex W introduces three levels including $W^{++/+}$, $W^{+/0}$ and $W^{0/-}$, whose energies are determined by the binding energies of the defects. At a minimum distance between the donor and the acceptor, the oxygen vacancy level shifts upward by 0.42 eV while the copper vacancy level shifts downward by 0.84eV as

shown in Figure 4.5 and the electronic levels of the complex states were chosen according to the experiments. According to this model, a negative V_{Cu}^{-} during its random walk associates with a single V_O^{+} to form a complex W^0. Unless this captures a hole to become a W^+, the complex, W^0 is not stable.

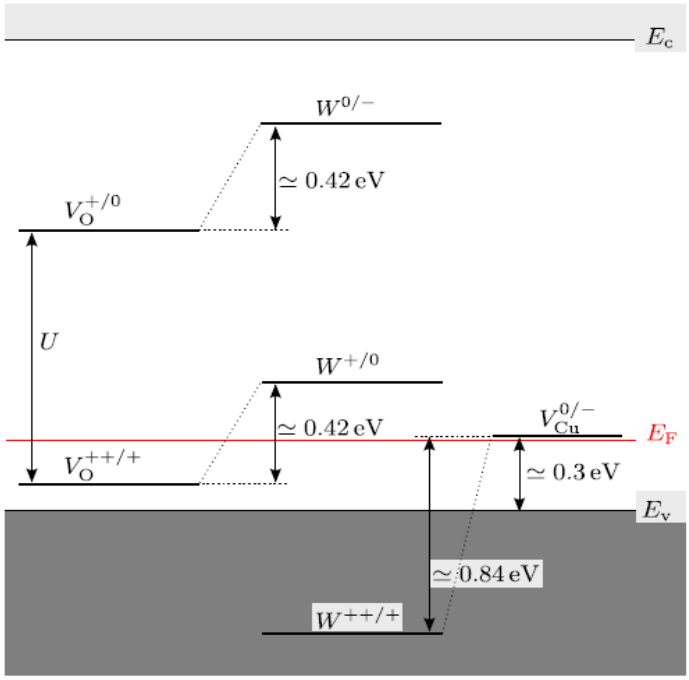

Figure 4.5 Representation of the defect electronic levels using acceptor-donor complex model [56].

Interpretation of the experimentally obtained N_D and N_A values using this model is explained as follows. For the sample kept at dark, V_{Cu} is identified as the acceptor and the donor in the new model is complex W^+. The N_A corresponds to the acceptor vacancy concentration $[V_{Cu}]$ and this number does not include the V_{Cu} which are bound to the complexes since they are not acceptors. N_D corresponds to the total number of oxygen vacancies in the complex. The total number of Cu vacancy concentration both bound and unbound is given as $[V_{Cu}]_{tot} = [V_{Cu}] + [V_O]_{tot}$. In order for Cu_2O to show p-type conduction, $[V_{Cu}]_{tot}$ should be always greater than $2[V_O]_{tot}$. Hence, for the dark sample, $[V_O]_{tot} = 4.92 \times 10^{14}$ cm^{-3} and $[V_{Cu}]_{tot} = 1.06 \times 10^{15}$ cm^{-3} according to the data from Table 4.1. When the sample is illuminated, the complexes

become neutral due to the capture of photo-generated electrons and many of them dissociates because they are unstable in the given temperature range. The isolated double charged oxygen vacancy emits a hole becoming a V_O^+ since the level $V_O^{++/+}$ is in valence band. While the donor concentration remained same as its concentration before the illumination because for one W^+ only one V_O^+ is formed from a W^+ upon light exposure, the concentration of Cu vacancies increased due to the dissociation of the neutral complex which was responsible for increase in conductivity. They also numerically solved the equation which relates to the rate of association of Cu vacancies with oxygen vacancies, which included five parameters -$[V_{Cu}]_{tot}$, $[V_O]_{tot}$, E_A, D_{VCu} (diffusion coefficient of Cu vacancy), and f_{diss} (fraction of dissociated complexes). Both vacancy concentrations agreed well with their experimental results as well with the numerical fits, but there was a strong discrepancy in their D_{VCu} results obtained from the experiments and the fit. They pointed out that the discrepancy was possibly from the fact that there was a significant error in their model or that the acceptor is something other than Cu vacancy and it has a lower diffusion coefficient than that of Cu vacancy.

4.3 Hypothesis and the design of experiments

As per our knowledge, there were no experiments to determine the chemical identity of the light induced metastable defects and there were no positron studies to study the open volume defects in Cu_2O under light till date. The observations from the PPC effect in Cu_2O showed that the conductivity increase was due to the increase of the acceptor concentration under light illumination. As shown from Chapter 3, PALS and DBS experiments can identify the open volume defects as well as its chemical nature. The variation of the vacancy size can be determined from the changes in positron lifetime. The lifetime increases as the size of the vacancy increases. Therefore, we can hypothesize that the average lifetime of Cu vacancies (chemical nature confirmed from our DBS experiments in chapter3) should decrease under light compared to the dark sample. Additionally, DBS would tell the chemical nature of the defects contributing to the PPC effect because the dissociation of the complex under light might

generate enough difference in the chemical environment PALS experiments were performed on three samples of Cu_2O powder (Alfa Aesar, 99.9%). The samples were first annealed at 400°C under vacuum to remove any metastable defects built-in during its fabrication process and equilibrated under dark condition at all times after annealing until positron measurements were performed. Sample 1 (S1) was equilibrated under dark for several days before measurements. Sample 2 (S2) was illuminated with a 60 W tungsten lamp before measurements and also during measurements. During the exposure to the light, the temperature was carefully monitored to avoid any heating from the irradiation. Finally, PALS was repeated for S2 as soon as S2 was placed under dark in order to verify that the influence of light on the positron lifetime due to the change of the free electron density in the bulk of Cu_2O. This measured is referred as Sample 3 (S3). DBS was performed on S1 and S2. Each measurement was repeated 2-3 times to test the reproducibility of the data. The information on the positron sources, spectrometers, and other electronics used in PALS and DBS was already provided in chapter 3.

4.4 Results and discussions

The results obtained from the measurements on the three samples which are positron lifetime (LT) values and vacancy contributions are presented in Tables 4.3 ~ 4.5. The positron annihilation data was first analyzed by fixing the bulk LT of Cu_2O (171 ps) in accordance with the analysis made in chapter 3 and other two LTs are left to vary freely to fit the data. The results of the analysis is shown in Table 4.3 and it shows three LT values for S1, 171ps, 326ps, and 2240ps with contribution of 48.81%, 50.71%, and 0.48% respectively. 326ps is possibly due to di-vacancies of Cu and possibly bigger clusters of Cu vacancies because there should be a high concentration of complexes of Cu vacancy under dark condition. The higher LT value 2240ps can be neglected due to its low intensity compared to other LTs. For S2, we observed 171ps, 256ps and 543ps with contribution of 0.1%, 92.5% and 7.4% respectively. Although 171ps was again attributed to the bulk annihilation, its contribution was too small and physically meaningless. This is considered as an artifact of the analysis because high contribution of

256ps indicated that there was an increase in the population of the identity that has a lower LT than 326ps observed from the sample kept under dark – we expect the identity to be the Cu vacancies with smaller size 'on average' than the average size under dark. As the average lifetime of the Cu vacancies becomes much closer to a true value of the bulk LT, the fitting process simply picked 256ps with high contribution instead of being able to separate the contribution properly between bulk and defect annihilation. In fact, the bulk LT was expected to decrease, if it occurs in any degree, upon light exposure because of the increase in the free electrons in the material due to band-to-band transition, which was not visible in the data from the illuminated sample. The overall behavior seems consistent with the hypothesis established earlier. S3 shows a similar behavior as S2 with LT values of 171ps, 272ps and 933ps with contribution of 7.1%, 90.9% and 2.07% respectively. Bulk LT shows a higher contribution of 7.1% compared to S2 and this may be due to the slow recovery of the metastable to the stable state.

Table 4.3 LT values from S1, S2 and S3 with a fixed bulk LT.

Sample	LT 1 (ps)	Intensity (%)	LT 2 (ps)	Intensity (%)	LT 3 (ps)	Intensity (%)
S1	171	48.81	(326±15)	50.71	(2240±20)	0.483
S2	171	0.1	(256±10)	92.5	(543±15)	7.4
S3	171	7.1	(272±12)	90.9	(933±10)	2.07

Because the analysis made with Table 4.3 suffered the artifact associated with the fixed bulk LT and the change in entire size spectrum of the Cu vacancies, the fitting was repeated without fixing the bulk LT and by using only two LTs as the fitting parameters as an attempt to present the overall change in the spectrum of Cu vacancies more effectively. Unlike the expectation, the average lifetime in the short time period (Lifetime 1) as well as its contribution varied little among S1~S3 regardless of the history of the samples and it was difficult to make

any meaningful discussion. Although the attempt was made to show the average change in the materials, having only two lifetimes in the fitting process significantly decreased the resolution.

Table 4.4 Two LT values from S1, S2 and S3 without fixing any LT.

Sample	LT 1 (ps)	Intensity (%)	LT 2 (ps)	Intensity (%)
S1	(260±5)	97.50	(850±15)	2.50
S2	(250±5)	94.10	(574±12)	5.9
S3	(262±5)	97.06	(811±8)	2.94

Finally, it was determined that using three LT parameters would provide better resolution and the fitting was repeated with three LT and without fixing bulk LT (Table 4.5). This time, the results clearly showed the average change in the defect population upon light exposure and the minimal effect of light-induced electron density increase in the bulk of materials. First, LT1 (198 ps) with a contribution of 69.6% for the dark sample increased to a higher LT of 250 ps with a higher contribution of 93.8% after illumination, which can be clearly explained by the increase in the concentration of smaller Cu vacancies including its mono vacancies. According to the hypothesis, after the light radiation the conductivity rise observed from the previous studies is due to higher concentration of the Cu monovacancies due to the dissociation of the complex V_{Cu} + V_{Cu}. Although further analysis and the modeling is possibly necessary to extract the precise size distribution of the Cu vacancies, the experiments confirmed that the average size of Cu vacancies was decreased to a smaller size upon light exposure potentially supporting the hypothesis. Furthermore, little change in LT1 as well as its contribution between S2 and S3 has indicated that the increase in the free electron density in the bulk of Cu_2O upon light exposure had little effect on the lifetime of the positron.

Table 4.5 Three LT values from S1, S2 and S3 without fixing any LT.

Sample	LT 1 (ps)	Intensity (%)	LT 2 (ps)	Intensity (%)	LT 3 (ps)	Intensity (%)
S1	(198±15)	69.6	(377±15)	30	(3590±20)	0.355
S2	(250±12)	93.8	(571±16)	2.4	(588±15)	3.9
S3	(256±14)	94.02	(581±15)	5.73	(5400±18)	0.259

Our data seems to follow the association and the dissociation of complexes of Cu vacancies, with the light radiation proposed by Kuzel et al [51-52]. However the defects responsible for the lower LT components due to dissociation of the complexes might be from V_{Cu}^{-} + V_{Cu}^{-}, or V_{Cu}^{-} + V_{O}^{+} depending on the concentration of the defects, as well as the fabrication of the sample. The DBS results shown in Figure 4.6 indicated there was little difference between the Doppler curves for the dark and the illuminated samples. The (S, W) parameters for S1 and S2 are (0.556, 0.0269) and (0.558, 0.0263) respectively. Although this requires further experiments and discussions, electron momentum distribution in Cu vacancies might be similar regardless of their sizes. In fact, this indirectly supported that the major defect complexes those respond to light were Cu vacancy complexes instead of Cu-O vacancy complexes proposed by Biccari et al [54, 56].

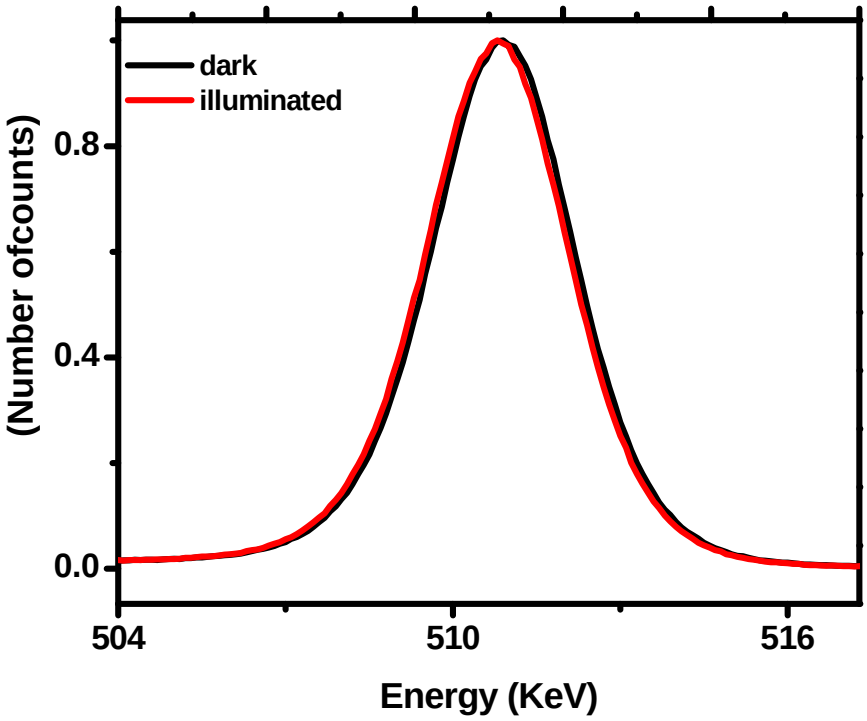

Figure 4.6 DBS spectra of Cu_2O sample before and after illumination.

4.5 Summary

Using PALS, we experimentally showed a signature of light induced metastable defects originated from the Cu-Cu complex which is obvious from a change in positron LT and defect population contributing to the LT change with and without light radiation. Our results are in accordance with that obtained by various groups previously due to PPC effect, by confirming our hypothesis stating that the conductivity rise during illumination is due to high concentration of Cu mono-vacancy concentration. The LT values of S1 and S2 are different showing a signature of defects caused by light illumination. Analysis with the three LT parameters for S1 showed a LT of 198 ps with a contribution of 69.6 % and S2 showed a LT value of 250 ps with a defect population contribution of 93.8 % attributed to increase in Cu mono-vacancy contribution. S2 and S3 showed similar LT values proving the bulk LT is not much affected by the light

radiation compared to the change in defect population and its impact to their lifetimes. The DBS results although did not show much difference between S1 and S2, but can conclude that no change in the chemical environment was identified because of the presence of majority of Cu-Cu complexes and not the Cu-O complex.

CHAPTER 5

INTRINSIC DEFECT STUDY IN Cu-BASED TRANSPARENT CONDUCTING OXIDES

5.1 Introduction

In this part of the study, several factors were investigated which play an important role in determining the electronic conductivity of the Cu-based delafossite compounds with a chemical formula of $CuM^{III}O_2$ including Cu_2O. Cu_2O was also explored since the delafossite compounds have the same valence band features as Cu_2O and could be used as a basic comparison how the conductivity changes by adding a M^{III} cation into the crystal structure. The particular effort was made for understanding the effect of M^{III} cation size on the vacancy formation energy in the compounds because it has been known that the vacancy defects in the compounds provide free holes in the conduction band and the concentration of the hole carriers is partially determined by the vacancy formation energy. Other factors which define the electronic structure of the delafossite compounds for example bond lengths between two Cu atoms affecting the defect formation energies were also discussed in this work.

Several groups attempted to explain the trend in conductivity and mobility with the presence of the M^{III} cation in the delafossite compounds. Nagarajan et al [40] explained the increased conductivity in few delafossite compounds is due to the smaller ionic radius of the M^{III} cation which leads to a better Cu d orbital overlap with the M^{III} states and hence a good hole conductivity. Scanlon et al [86] demonstrated the importance of increased covalency between the M^{III} states and oxygen as the size of the M^{III} cation increases. The above arguments discussing the affect of the M^{III} cation provided us a motivation to calculate the defect formation energy of intrinsic defects in delafossite compounds, which could provide further insight to calculate the concentration of the acceptors. There have been a number of studies to calculate the formation energies of intrinsic defects in delafossite compounds using local density

approximations (LDA) [57-61], but to the best of our knowledge till date the affect of M^{III} cation on the defect formation energies has not being investigated. In an attempt we employed the generalization of Van Vechten Cavity Model (VVCM) to calculate formation energy of neutral intrinsic defects. VVCM uses several input parameters such as bond lengths, band gaps, unit cell parameters and covalent or ionic radii. Hence using VVCM it could be readily seen that the affect of the above mentioned parameters on the vacancy formation energies and the parameters actually define the electronic structure on the vacancy formation energies. Introduction to VVCM is given in detail in section 5.2. As discussed in the explanation above electronic structure of the delafossite compounds play an important role in determining the conductivity properties. Similarly in this study we wanted to explore how the electronic structure affects the defect formation energies of intrinsic defects of few Cu-based delafossite compounds ($CuAlO_2$, $CuInO_2$ and $CuCrO_2$). The properties of these delafossite compounds have been introduced in chapter 1 some of which include p-type conductivity, wide band gap which are very essential in fabrication p-n heterojunctions. P-type transparent conducting oxides (TCO) are important since majority are n-type and wide band gap(≥2.5) become essential for a high transparency(≥85%) novel TCO applications. CuInO2 showed a bipolar (both p-type and n-type) conduction and a large direct band gap (3.12eV) [87] compared to other delafossite compounds and could be material of interest in the field of p-n homojunctions. $CuCrO_2$ on the other hand showed a very high conductivity (220 S cm^{-1}) [44] when doped with an extrinsic dopant and is a material of growing interest in the field of delafossite compounds. $CuAlO_2$ is the parent p-type delafossite compound fabricated by Kawazoe et al [23-24] with a wide band gap (2.75eV) [86] and its electrical properties are always compared to other delafossites. Hence we chose $CuAlO_2$, $CuCrO_2$, $CuInO_2$ along with Cu_2O for our defect study.

Though we calculate the defect formation energies of other intrinsic defects in the above mentioned compounds our focus is on the effect of M^{III} cation size of the defect formation energy of Cu vacancies(V_{Cu}). V_{Cu} are major acceptor type defects due to their low formation

energies and shallow ionization levels in delafossite compounds and Cu_2O which give rise to p-type conduction. The equilibrium concentration of V_{Cu} in Cu_2O is found close to the experimentally observed concentrations ranging between 2 $X10^{18}$ cm^{-3} and 2 X 10^{20} cm^{-3} [88]. Please refer to Table 1.1 for comparison of Cu vacancy formation energies and ionization levels of other delafossite compounds.

5.2 Theory of VVCM

5.2.1 Introduction

According to VVCM [89], for any semiconductor a vacancy, V_X is considered as a macroscopic cavity having a surface area, 'A' as determined by the equilibrium shape of the cavity. Its formation energy (ΔH_f) is given by the combination of the surface energy predicted from the density of 'free' valence electrons [90] and the bonding energy due to the short-range covalent force [91-95]. In its mathematical expression

$$\Delta H_f\ (V_x) = AE_s^m + E^b \tag{5.1}$$

where E_s^m explains the metallic contribution of its surface enthalpy and E^b is the heat of bonding, which could be determined both experimentally and theoretically.

To calculate the surface area of the cavity 'A' we need to assume that the vacancy cavity has its equilibrium shape. The surface area of the cavity and its volume is defined by the dimensions of the Wigner-Seitz radius (r_w). When a vacancy cavity is created by removing an atom from the crystal lattice the equilibrium shape changes since the surface energy of this cavity is a function of the orientation of the crystal. Hence the surface areas of vacancy cavities are always larger than the areas of the equilibrium shape and need to be multiplied by a geometrical factor to the spherical areas. For example, the shape of the vacancy cavities in Si and Ge are octahedral. The shape of the vacancy cavity is obtained by drawing a Wigner-Seitz surrounding the vacancy atom. The geometrical factor of 1.18 is determined by equalizing the spherical volume to the vacancy cavity volume [89].

5.2.2 Surface plasmon theory to determine E_s^m [90]

When a surface is newly created inside a material due to the collective motion of the electrons, the surface energy defined as E_s^m arises. According to this theory, when a separation occurs by splitting the crystal by a distance, 'd' a pair of surface modes have been created from the bulk material defined by longitudinal plasmon frequency ω_L and a transverse plasmon frequency ω_T. The motion of the collective modes whose direction is defined by a wave vector 'k', is parallel to the surface. Now when the two created surfaces are further pulled off to an infinite distance, there is asmall adhesion energy to replace the new bulk modes. The above phenomenon is illustrated in Figure 5.1. Hence the metallic contribution to the surface energy is given by the following expression

$$E_s^m = \frac{\sqrt{2}-1}{16\pi} h\omega_p k_c^2 = C r_s^{-5/2} \tag{5.2}$$

where 'ω_p' is the bulk plasmon frequency and k_c is the surface plasmon cutoff wave vector and C is the universal constant, and r_s is the density parameter and is given by the following equation

$$r_s = \left(\frac{3}{4\pi}\right)^{1/3} \left(\frac{V}{Nv}\right)^{1/3} \tag{5.3}$$

where V is the volume of the unit cell which has N atoms and v is the number of free valence electrons.

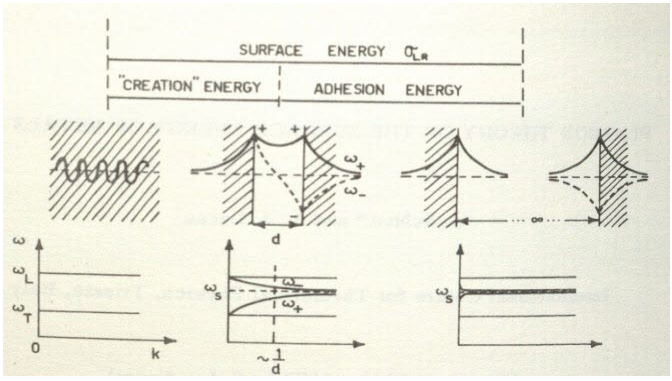

Figure 5.1 Dispersion relation for bulk solid with two branches of surface plasmon modes showing how the surface energy changes before splitting the crystal into two and after with respect to the plasmon modes [90].

5.2.3 Penn-Philips Model to determine E^b [89, 91-92]

The enthalpy of a semiconducting phase relative to the jellium model reference will be defined as the heat of bonding (E^b). The jellium- metal reference state is a good choice when we approach the study of semiconductors from the nearly–free electron approximation. Hence to calculate E_b we use the isotropic - Penn – model which is a highly simplified approximation of a semiconductor, where the true electronic band structure and Brillouin zone are replaced by a spherically symmetric structure and zone with a symmetric band gap, E_g as shown in Figure 5.2. E_g is adjusted such that the optical dielectric constant, approaches the band gap in the long wavelength limit and is given as follows.

$$\epsilon_0 = 1 + \left(\frac{h\omega_p}{E_g}\right)^2 \left[1 - B + \frac{1}{2}B^2\right] \tag{5.4}$$

where ω_p is the plasma frequency of the free electron gas and is equal to $\left(4\pi N_e e^2/m_e\right)^{1/2}$ (m_e and e are the rest mass of the electron and its charge respectively). B is given by the Equation 5.5,

$$B = \frac{E_g}{4E_{F,jm}} \tag{5.5}$$

Where $E_{F,jm}$ is the Fermi energy of a free electron gas or the jellium metal reference state having the same electron density as the valence electron density of the semiconducting phase.

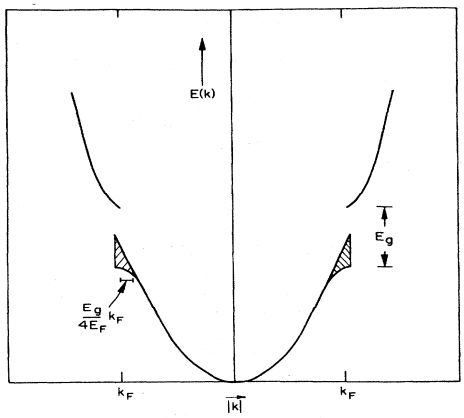

Figure 5.2 Electronic band structure based on the Penn-Philips model showing the energy ($E_g/4E_f$) of the idealized semiconductor (shaded area) [89, 91-92].

The total energy of all occupied, valence band states of a semiconductor based on the Penn-Philips model which is referred to the heat of bonding (E_b) is always less than that of the jellium metal (E_{jm}) for which the band structure is a free electron parabola with the same bottom of band energy. The crystal potential which produces the band gap pushes the valence band states below the energy of the free electron gas as it pushes the conduction band states above that energy, but only the valence band states are occupied. If the bottom of the band energies is assumed to be same, the energy of the model semiconductor would be less than the energy of the jellium metal by the amount indicated in the shaded area of Figure 5.2. Van Vechten [89] calculated the energy(heat of bonding) due to the opening of the band gap and the formation of the bonds exactly and analytically given by the following equation.

$$E^{\,b} = -E_{F,jm}\left[3B^2\left(1+\ln\left({}^{B}/_{2}\right)\right)-4B^3\right] \tag{5.6}$$

5.3 Calculations of Wigner-Seitz radii

To calculate the surface energy and surface area of the vacancy cavity Wigner-Seitz radii should be determined first. Polyhedral structure of the cavity can be found by assuming there is no structural relaxation in the crystal structure during vacancy formation. Using the equations [5.7] ~ [5.10], we solved Wigner-Seitz radii of r_w^{Cu}, r_w^{O} and $r_w^{M^{III}}$ corresponding to Cu,

O and M^{III} atoms respectively by assuming that the ratio of the Wigner-Seitz radii is equal to the ratio of the ionic radii (IR) and the total volume of the unit cell is equal to the addition of all the Wigner-Seitz cells in the unit cell.

$$r_{ion}^{Cu} / r_{ion}^{O} = r_{w}^{Cu} / r_{w}^{O} \quad (5.7)$$

$$r_{ion}^{M^{III}} / r_{ion}^{O} = r_{w}^{M^{III}} / r_{w}^{O} \quad (5.8)$$

$$V = N_{Cu} V_{w}^{Cu} + N_{O} V_{w}^{O} \quad \text{(for } Cu_2O\text{)} \quad (5.9)$$

$$V = N_{Cu} V_{w}^{Cu} + N_{O} V_{w}^{O} + N_{M}{}^{III} V_{w}^{M^{III}} \quad \text{(for } CuM^{III}O_2\text{)} \quad (5.10)$$

In the equations, V is the volume of the unit cell, V_w^X is the spherical volume of the Wigner-Seitz cell for each atom, and N_X (x=Cu, O, M^{III}) is the number of the particular atoms in the unit cell of Cu_2O and $CuM^{III}O_2$. r_{ion}^{Cu},r_{ion}^{O},$r_{ion}^{M^{III}}$ are the ionic radii of the Cu, O & M^{III}ions respectively. The structure parameters which include the lattice constants (a, c and u in units of Å), bond lengths, ionic radii (IR) and the total volume of the unit cells of Cu_2O and $CuM^{III}O_2$ were taken from the X-ray diffraction data in the literature [96-98,86,77] and are compiled in Table 5.1.

Table 5.1 Structural information of Cu_2O and delafossites from the literature.

*DFC	Lattice parameters a(Å)	c(Å)	u(Å)	Vol.(Å^3)	Cu-O (Å)	M^{III}-O (Å)	Cu-Cu (Å)	IR(Å)		
								Cu	O	M^{III}
CIO	3.29	17.38	0.105	163.21	1.84	2.17	3.29	0.46	1.38	0.80
CCO	2.97	17.10	0.106	130.72	1.84	2.03	2.97	0.46	1.38	0.61
CAO	2.86	16.95	0.109	120.18	1.86	1.93	2.86	0.46	1.38	0.53
Cu_2O	4.27			77.85	1.85		3.04	0.5	1.35	

**Notation in the table used for labeling delafossite compounds (DFC),*

$CuInO_2$(CIO),$CuCrO_2$(CCO),$CuAlO_2$(CAO).

The cubic structure of Cu_2O shown in Figure. 5.3 which includes Cu and O vacancy cavities – the shape of the O vacancy cavity is a tetrahedron, and a Cu vacancy cavity has an octahedral shape. The crystal structure of the delafossites is shown in Figure. 5.4 including Cu, M^{III}, and O vacancy cavities with the shape of a dodecahedron, an octahedron, and a tetrahedron respectively.

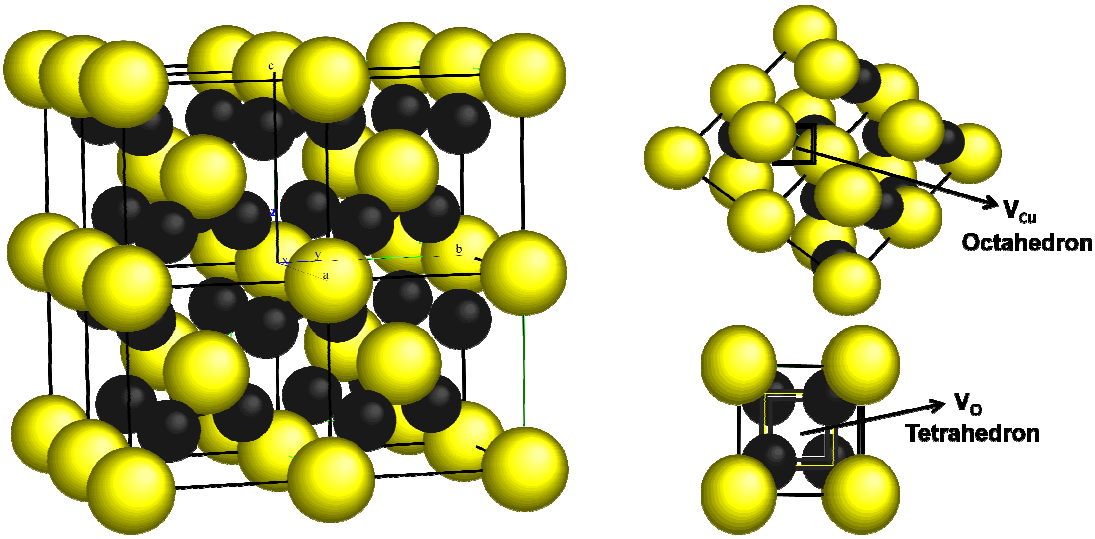

Figure 5.3 Crystal structure of Cu_2O along with the vacancy cavities of Cu-octahedron and O-tetrahedron. Each atom is color-coded (Cu - yellow; O- black).

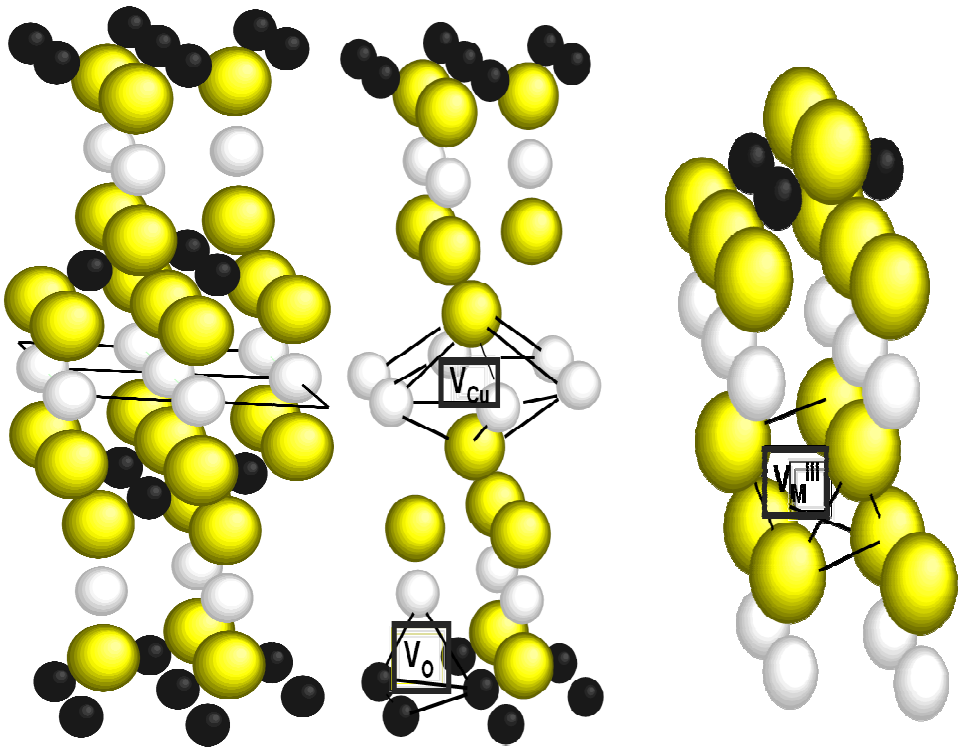

Figure 5.4 Crystal structures of delafossites along with the vacancy cavities of Cu-dodecahedron, O-tetrahedron and M^{III}-octahedron. Each atom is color-coded (Cu - yellow; O-black; M^{III} - grey).

5.4 Results and discussion

The calculated values of the defect formation energies of , are shown in Table 5.2 along with their metallic contributions and covalent contributions of the total formation energies. The defect formation energies of the Cu vacancy is ranked as $Cu_2O<CuInO_2<CuCrO_2<CuAlO_2$ discussion will focus on the defect formation energy of V_{Cu} since it is the major acceptor defect in the Cu-based oxides as mentioned in the earlier part of the introduction section. of V_{Cu} is of the order of $Cu_2O<CuInO_2<CuCrO_2<CuAlO_2$ and E_b is the order of $Cu_2O<CuInO_2<CuCrO_2<CuAlO_2$ and the values are shown in the table. The two major factors which determine the are the size of Wigner-Seitz cell and the volume of the unit cell. Because VVCM predicts the area-normalized to be uniform throughout the

material with the free valence electrons governing the entire bonding, the larger the Wigner-Seitz radii (WSR), the larger the surface area of the cavity and the bigger the energy is needed to create a vacancy. For both Cu_2O and delafossite, the Wigner-Seitz radii depend on the ionic radii of the Cu, O & M^{III} ions and as the size of the M^{III} ion decreases the lower the surface area of the cavity and as the volume of the unit cell gets smaller the AE_s^m increases hence the order of metallic component thus obtained $Cu_2O<CuInO_2<CuCrO_2<CuAlO_2$. Hence our calculations showed that as M^{III} cat-ion size increases AE_s^m decreases.

Table 5.2 Calculated defect formation energies of vacancies in Cu-based oxides.

Compound	V_X	$\Delta H_f(V_X)$ (eV)	AE_S^m (eV)	$A(Å)^2$	E_s^m (10^{15} eV/cm^2)	(WSR) r_w(Å)	E_b (eV)
$CuInO_2$	V_{Cu}	1.81	0.30	6.0	0.66	0.66	1.51
	V_{In}	2.54	1.03	15.64	0.66	1.05	1.51
	V_O	5.52	4.01	60.76	0.66	1.79	1.51
$CuCrO_2$	V_{Cu}	2.15	0.39	4.88	0.80	0.56	1.76
	V_{Cr}	2.42	0.66	8.33	0.80	0.75	1.76
	V_O	6.03	4.27	53.45	0.80	1.69	1.76
$CuAlO_2$	V_{Cu}	2.3	0.40	4.71	0.86	0.55	1.90
	V_{Al}	2.43	0.53	6.21	0.86	0.65	1.90
	V_O	6.33	4.43	51.56	0.86	1.66	1.90
Cu_2O	V_{Cu}	1.40	0.40	8.33	0.49	0.75	1.0
	V_O	4.78	3.78	74.38	0.49	2.03	1.0

In the previous section the dependence of the Wigner-Seitz radii, the volume, the surface areas of the vacancy cavity on the surface energy which is the metallic contribution of the total defect formation energy of the cavity was discussed. The results obtained from the covalent contribution are discussed as follows. This energy which is denoted by E_b called the heat of bonding is calculated using the isotropic-Penn model as discussed in the above section.

The band gap E_g was calculated from the dielectric constant ε which was known from the literature and Fermi energy E_F of the free electron gas.

As shown in the Table 5.3, the E_b values obtained from the calculations is the order of $Cu_2O<CuInO_2<CuCrO_2<CuAlO_2$. The volume of the unit cell gets bigger as the size of the M^{III} cation in the delafossite compounds increases. This might be due to the stacking of the M^{III}-O layers in the crystal structure making the volume bigger. If volume of the unit cell gets bigger we obtain low E_g and E_F values, since these values depend on the density of the free valence electrons as shown in the equations 5.4 and 5.5. Higher contribution from the valence electrons interacting with the M^{III} cation gives a lower E_b value. For Cu_2O, since there is no M^{III} cation present and hence the volume of the unit cell is smaller than the delafossite compounds and the number of valence electrons is smaller and hence obtain low E_g and E_F values. From our calculations it clearly shows that as M^{III} cat-ion size increases E_b decreases in the order of $Cu_2O<CuInO_2<CuCrO_2<CuAlO_2$.

Table 5.3 Calculated E_g and E_F according to the dielectric constants from the literature [99-102]

Compound	E_F(eV)	E_g(eV)	Dielectric constant ϵ
$CuInO_2$	15.97	9.7	5.5
$CuCrO_2$	18.69	10.3	5.46
$CuAlO_2$	19.76	11.2	5.1
Cu_2O	12.47	6.32	7.11

The bond length between Cu atoms (Table 5.1) also is an important factor in determining the defect formation energies of Cu vacancies in delafossites. It was observed in the previous work, Cu_2O has a lower formation energy of Cu vacancy than $CuAlO_2$ because three-dimensional Cu-Cu interaction in Cu_2O makes it easier to form V_{Cu} compared to the two dimensional network of $CuM^{III}O_2$ [2]. This emphasizes that both the proximity of Cu atoms and the dimensionality of the Cu-Cu interaction affects the defect formation energies of Cu

vacancies in Cu_2O and its derived compounds from our calculations. According to Table 5.1, as the size of the M^{III} ion increases, the Cu-Cu and Cu-O-Cu bond lengths increase and cause larger volume deformation, hence a higher chance of hole hopping via channels Cu-Cu or Cu-O-Cu The total formation energy of V_{Cu} which is a sum of AE_s^m and E_b is of the order of $Cu_2O<CuInO_2<CuCrO_2<CuAlO_2$. From our calculations as the size of the M^{III} ion increases the defect formation energy of Cu vacancy decreases. The carrier concentration of Cu vacancies can be estimated from the defect formation energies and from our results the defect concentrations would be the order of $Cu2O>CuInO_2>CuCrO_2>CuAlO_2$. Discussion on the hole mobilities in the delafossites can be further supported by the theoretical calculations. The effective mass (m^*) is given as follows

$$\frac{1}{m^*(E)} = \frac{1}{h^2 k}\frac{dE}{dK} \tag{5.11}$$

where E(k) is the band edge energy of the wave vector k, which can be obtained from different methods of LDA calculations. Table 5.4 shows the hole effective masses of $CuCrO_2$, $CuAlO_2$ [86], and $CuInO_2$ [103]. They were calculated along [100], [010] and [001] directions. The table particularly shows that $CuAlO_2$ and $CuCrO_2$ have relatively large hole effective masses along [001] compared to [100] and [010] while the effective masses along [100] and [010] directions are isotropic for all three compounds. The authors of the studies, therefore, explained that the holes are expected to hop from Cu to Cu in $CuCrO_2$ and $CuAlO_2$ while the hole conduction in $CuInO_2$ is likely to occur along the $M^{III}{}_3O_2$ layer due to its low effective mass along [001] direction. The mobility of $CuInO_2$ is also expected to higher than those of $CuCrO_2$ and $CuAlO_2$ due to its lower effective mass. It's an intriguing physical question why there is a huge difference in the effective mass along the [001] direction in those compounds as the theoretically calculated results only explain numerically.

Table 5.4 The theoretically calculated effective hole masses of $CuInO_2$, $CuCrO_2$, and $CuAlO_2$ in the units of free electron mass along [100], [010] and [001] planes [86,103].

Compound	m_{100}	m_{010}	m_{001}
$CuAlO_2$	2.60	2.60	58.43
$CuCrO_2$	2.96	2.96	7.21
$CuInO_2$	3.22	3.22	0.68

Recent work of Scanlon et al [86] discussed the order of degree of covalency between the M^{III} cation and oxygen in the delafossite compounds affect the conductivity properties. According to the local density approximation (LDA) studies in the literature [86, 103], the order of degree of covalency between the M^{III} cation and oxygen in the delafossite compounds presented in this study follows as, Cr-O < In-O < Al-O from their calculated Bader partial electron charges (Table 5.4). As shown in the table, the charge of Cr, In, Al is +1.68, +1.83, +2.48 respectively and the charge for O of the three compounds are -1.10, -1.17 and -1.50 respectively, which indicates Cr-O are less ionic than In-O and Al-O. Al and O are most ionic among them, hence there is no major covalent mixing of the Al states with the O 2p states. Whereas Cr states have the highest covalent interactions with O 2p states in the valence band giving rise to higher carrier mobility $CuCrO_2$ than the other compounds. In-O are less ionic compared to Al-O according to the calculated charges. The degree of covalency trend follows the experimental conductivity trend ($CuCrO_2$>$CuInO_2$>$CuAlO_2$).

Table 5.5 Bader partial electron charges for $CuCrO_2$, $CuInO_2$ and $CuAlO_2$ calculated using LDA [86, 103].

Compound / Atom	$CuCrO_2$	$CuInO_2$	$CuAlO_2$
Cu	+0.52	+0.50	+0.52
M^{III}	+1.68	+1.83	+2.48
O	-1.10	-1.17	-1.50

So far from the previous work and VVCM calculations the parameters which define the crystal structure of Cu-based oxides affect the defect formation energy of Cu vacancy, carrier concentration of the holes, mobility and conductivity.

Since VVCM uses many approximations and depends mainly on the observed and theoretically calculated parameters like band gaps, lattice parameters, bond lengths and ionic radii, calculations of Cu vacancy defect formation energies in delafossite compounds and Cu_2O are not really close to LDA calculations but follow the trend as shown in the Table 5.6 for comparison.

Table 5.6 Formation energies of Cu vacancies in $CuAlO_2$ [2], $CuCrO_2$ [60], $CuInO_2$ [61] calculated using LDA in comparison with the calculated results obtained in this study using VVCM.

Compound	Formation energy of V_{Cu} (eV)	
	LDA	VVCM
$CuAlO_2$	0.98	2.3
$CuCrO_2$	0.95	2.15
$CuInO_2$	0.49	1.81

5.5 Summary

Using VVCM we calculated the defect formation energies of intrinsic defects in Cu-based p-type delafossite oxides. We show that the size of the M^{III} cation plays a major role in determining V_{Cu} formation energies. The larger the ionic size the smaller the Cu vacancy formation energy observed and follows the order as [Cu_2O (1.40eV) < $CuInO_2$ (1.81eV) <$CuCrO_2$ (2.15eV) < $CuAlO_2$ (2.3eV)]. The individual contributions [the metallic(AE^S_m) and the covalent (E_b)] in determining the total formation energy also have been affected by the size of the cation, since Wigner-Seitz radii and volume of the unit cell are the major factors in the calculation of metallic and covalent contributions respectively which depend on the ionic radii of the M^{III} cation. The bond lengths between Cu-Cu are observed to affect the Cu vacancy formation energies from our calculations. The larger the Cu-Cu distance the easier to form V_{Cu} and hence a low defect formation energy and follow the trend [$CuInO_2$ (1.81eV) < $CuCrO_2$ (2.15eV) < $CuAlO_2$ (2.3eV)]. We found higher formation energies for oxygen vacancies and hence do not contribute for the conduction due to their low concentrations. The defect formation energies for the other intrinsic defects is of the order of $V_{M^{III}} < V_O$ in all the delafossites depends majorly on the surface areas of the cavities.

CHAPTER 6

CONCLUSIONS AND FUTURE WORK

6.1 Conclusions

Two main objectives in this research are to identify the chemical nature of the major intrinsic structural defects in Cu_2O primarily using positron annihilation lifetime spectroscopy (PALS) and Doppler broadening spectroscopy (DBS) and to calculate the defect formation energies of intrinsic defects in p-type Cu-based TCO materials by employing Van Vechten cavity model (VVCM) in order to explain their electronic conductivities. The defects play an important role in determining the majority carrier type, carrier mobility and its and its concentration.

The strong presence of copper vacancy (V_{Cu}) and its clusters in copper oxides were identified using their characteristic lifetimes and was further supported by the analysis of Doppler broadening and photoluminescence measurement. The difference observed in the DBS spectra of Cu_2O and CuO also revealed the change in the momentum distribution of electrons participating in the positron annihilation between them, and it was systematically explained by the degree of hybridization between Cu 3*d* and O 2*p* states. The S-W plot also confirmed that the dominant presence of Cu vacancies in the copper oxides.

Persistent photoconductivity (PPC) observed in Cu_2O has been a primary cause for the time-dependent instability of the electronic devices made of Cu_2O and one classification of the theory has been explaining PPC using the dissociation of the vacancy complexes upon light exposure and their slow recovery. Again, PALS and DBS were used in this study in order to identify the light-induced meta-stable vacancies. For the first time in this field, we showed a direct evidence of the metastable vacancies using the positron lifetime analysis. The increase in the defect population contributing to Cu mono vacancies after light radiation as compared to

before illumination showed that copper vacancy complexes dissociated under light. The DBS showed no difference between the dark and the illuminated samples, indicating that the chemical identity of the dominant vacancies in the sample before and after illumination remained similar while its size spectrum could change upon light exposure, which further supported the dissociation of copper vacancy complexes under light PALS also verified that the increase of the free electron density in the bulk of Cu_2O upon light exposure had a minimal effect on the lifetime of positron and the change observed was mostly from the change in the size spectrum of Cu vacancies.

In Cu-based delafossites, we identified V_{Cu} as the major acceptor due to its low formation energy – it had the lowest formation among other mono-vacancies and it was followed by the formation energies of V_M^{III} and V_O in order. The M^{III} size effect on V_{Cu} formation energy was studied using Van Vechten cavity model (VVCM). The calculation showed that the larger the ionic radius of M^{III} cation is, the lower V_{Cu} formation energy is. The calculation showed further that the bond length between Cu-Cu was another important factor, which affects the V_{Cu} formation energy in Cu-based delafossites. The larger the distance of Cu-Cu is, the easier to form V_{Cu} in the delafossite compounds it becomes. It should be noted though that, even though Cu-Cu distance in Cu_2O is smaller than that of $CuInO_2$, the formation energy of V_{Cu} in Cu_2O was lower than $CuInO_2$.

6.2 Future work

To confirm the theoretically calculated V_{Cu} formation energy in Cu_2O, it is possible to calculate the concentration of Cu vacancies at different temperatures by analyzing the positron annihilation data obtained at those temperatures. The experiments need to be designed to determine trapping coefficient using an individual reference method for Cu vacancies and eventually to determine positron trapping rate. More experiments using PALS and DBS can be performed to see how the size of the vacancy and the vacancy concentrations vary in Cu_2O to further support our existing results. This could be explored by measuring the positron lifetime

change as a function of temperature, since temperature can change the defect size and concentrations.

Theoretical calculations of positron lifetime would further confirm our PALS results since lifetime values are mainly dependent on the statistics, the fitting of the spectrum, and several other instrument-related parameters including resolution, source and background correction etc. We could make a concrete estimate of defect concentrations of Cu vacancies and other intrinsic defects using vacancy formation energies from VVCM and compare with existing observed results. The defect formation energies of intrinsic defects using VVCM could be applied to other binary and ternary oxides including ZnO and In_2O_3 in order to study how their crystal structures affect the formation energies and VVCM is a simple way to estimate. Since VVCM is limited to few compounds with a particular electronic configuration for the covalent contribution of defect formation energies, a more generalized model of VVCM has to be developed which could be applied to other compounds. The VVCM calculation can be also improved by designing experiments to measure the heat of bonding (E_b) from the actual material because the theoretical calculations of E_b performed in this study used the dielectric constant of the material off the literature, which, we think, might be a source of error in our calculations.

REFERENCES

1. H. Raebiger, S. Lany, and A. Zunger, Phys. Rev. B **76**, 045209 (2007).
2. M. Nolan, Thin Solid Films **516**, 8130 (2008).
3. D. O. Scanlon and G. W. Watson, J. Phys. Chem. Lett. **1**, 2582 (2010).
4. W. Wang, D. Wu, Q. Zhang, L. Wang, and M. Tao, J. Appl. Phys. **107**, 123717 (2010).
5. R. M. de la Cruz, R. Pareja, L. Diaz, and J. V. Garcia-Ramos, Solid State Commun. **71**, 93 (1989).
6. N. Nancheva, P. Docheva, and M. Misheva, Mater. Lett. **39**, 81 (1999).
7. F. Biccari, C. Malerba, and A. Mittiga, Proc. of the 23rd European Photovoltaic Solar Energy Conference, Valencia, Spain, 2008 (WIP, Munich, 2008), p. 583.
8. Jerome D. Schick, Dan Trivich, J. Electrochem. Soc. **119**, 376 (1972).
9. M. Tapiero, J. P. Zielinger, C. Noguet, Physica. Status. Solidi. (a), **33**, 155 (1976).
10. K. Badekar, Ann. Phys. (Leipzig) **22**, 749 (1907).
11. C. M. Lampert, Sol. Energy Mater. **6**, 1 (1981).
12. K. L. Chopra, S. Major, D.K. Pandya, Thin Solid Films **102**, 1 (1983).
13. I. Hamberg, C.G. Granqvist, J. Appl. Phys. **60,** R123 (1986).
14. D. S. Ginley, C. Bright, MRS Bull. **15**, (2000).
15. H. L. Hartnagel, A.L. Dawar, A.K. Jain, C. Jagadish, Semiconducting Transparent Thin Films, IOP Publishing Ltd., Bristol and Philadelphia, 1995.
16. R. G. Gordon, MRS Bull. **52**, (2000).
17. B. G. Lewis, D.C. Paine, MRS Bull. **22**, (2000).
18. A. J. Varkey, A. F. Fort, Thin Solid Films **239**, 211 (1994).
19. G. Haacke, Ann. Rev. Mater. Sci. **7**, 73 (1977).

20. R.J. Hill and S.J. Nadel, Coated Glass Application and Markets, 1st ed. (British Oxygen Coating Technology, Fairfield, CA, 1999) p. 143.
21. Toshio Kamiya and Masashi Kawasaki, MRS Bull. **33**, 1061 (2008).
22. A. Tsukazaki, A. Ohtomo, M. Kawasaki, Appl. Phys. Lett. **88**, 152106 (2006).
23. Hiroshi Kawazoe, Hiroshi Yanagi, Kazushige Ueda, and Hideo Hosono, MRS Bull. 28 (2000).
24. Hiroshi Kawazoe, Masahiro Yasukawa, Hiroyuki Hyodo, Masaaki Kurita, Hiroshi Yanagi & Hideo Hosono, Nature, 389, 939 (1997).
25. D. Look, Mat. Sci. Eng. B, **80**, 383 (2001).
26. A. Tsukazaki, M. Kubota, A. Ohtomo, T. Onuma, K. Ohtani, H. Ohno, S. F. Chichibu, M. Kawasaki, Jpn. J. Appl. Phys. **44**, L643 (2005).
27. C. Persson, A. Zunger, Phys. Rev. B, **68**, 073205 (2003).
28. H. Hiramatsu, K. Ueda, H. Ohta, M. Hirano, M. Kikuchi, H. Yanagi, T. Kamiya, H. Hosono, Appl. Phys. Lett. **91**, 012104 (2007).
29. H. Mizoguchi, M. Hirano, S. Fujitsu, T. Takeuchi, K. Ueda, H. Hosono, Appl. Phys. Lett. **80**, 1207 (2002).
30. T. Kamiya, S. Narushima, H. Mizoguchi, K. Shimizu, K. Ueda, H. Ohta, M. Hirano, H. Hosono, Adv. Funct. Mater. **15**, 968 (2005).
31. J. Ghijsen, L.H. Tjeng, J. van Elp, H. Eskes, J. Westerink, G.A. Sawatzky, M.T. Czyzyk, Phys. Rev. B, **38**, 11322 (1988).
32. B.J. Ingram, G.B. Gonzalez, D.R. Kammler, M.I. Bertoni, T.O. Mason, J. Electroceram. **13**, 167 (2004).
33. R. W. G. Wyckoff, Crystal Structures, 2nd ed., (Interscience, New York, 1963).
34. B. U. Köhler and M. Jansen, Z. Anorg. Allg. Chem. **543**, 73 (1986).
35. F. A. Benko, F. P. Koffyberg, J. Phys. Chem. Solids, **45**, 57 (1984).

36. R. E. Stauber, J. D. Perkins, P. A. Parilla, D. S. Ginley, Electrochem. Solid State Lett. **2,** 654 (1999).

37. B. J. Ingram, T. O. Mason, R. Asahi, K. T. Park, A. J. Freeman, Phys. Rev. B, 64, 15 (2001).

38. H. Katayama-Yoshida, T. Koyanagi, H. Funashima, H. Harima, A. Yanase, Solid State Commun. **126**, 135 (2003).

39. R. Nagarajan , N. Duan , M.K. Jayaraj , J. Li , K.A. Vanaja , A. Yokochi , A. Draeseke , J. Tateb, A. W. Sleight, Int. J. Inorg. Mater, **3,** 265 (2001).

40. R. Nagarajan, A. D. Draeseke, A. W. Sleight, and J. Tate, J. Appl. Phys. **89**, 8022 (2001).

41. S. J. Fonash, editor, Solar cell device physics, New York: Academic Press, (1981) p. 80.

42. M. Nolan, S.D. Elliott, Phys. Chem. Chem. Phys. **8**, 5350 (2006).

43. F. A. Benko and F. P. Koffyberg, J. Phys. Chem. Solids **48**, 431 (1987).

44. M. A. Marquardt, N. A. Ashmore, and D. P. Cann, Thin Solid Films **496**,146 (2006).

45. Brattain, W. H. The copper oxide rectifier. Review of Modern Physics, **23,** 203 (1951).

46. Pollack, G. P. and Trivich, D.Journal of Applied Physics, **46,** 163 (1975).

47. Porat, O. and Riess, Solid State Ionics, **81,** 29 (1995).

48. Bloem, J., Van der Houven van Oordt, A. J., and Kröger, F. A., Physica, **22,** 1254 (1956).

49. Papadimitriou, L., Dimitriadis, C. A., Dozsa, L., and Andor, L. Solid-State Electronics, **32,** 445 (1989).

50. Mittiga, A., Salza, E., and Sarto, F. Proceedings of 21st European Photovoltaic Solar Energy Conference, Dresden, Germany, p. 219 (2006).

51. J. Pastrnak, R. Kuzel, Czech. J. Phys. **6**, 217 (1956).

52. R. Kuzel, Czech. J. Phys. 8, 81 (1958).

53. Jerome D. Schick, Dan Trivich, J. Electrochem. Soc. **119**, 376 (1972).

54. A. Mittiga, F. Biccari, C. Malerba, Thin Solid Films, **517**, 2469 (2009)

55. J. P. Zielinger, C. Noguet, M. Tapiero, *Physica. Status. Solidi. (a),* **42**, 91 (1977).

56. F. Biccarri, Ph.D Thesis, University of Rome, 2009.

57. I. Hamada and H. Katayama-Yoshida, Physica B **376**, 808 (2006).

58. F. Zhi-Jie, S. Li-Jie, and L. Yong-Hui, Chin. Phys. B **17**, 4279 (2008).

59. Z. J. Fang and L. J. Shi, Phys. Lett. A **372**, 3759 (2008).

60. David O. Scanlon and Graeme W. Watson, J. Mater. Chem. 21, 3655 (2011).

61. Liu Li, Masters Thesis. National University of Singapore, Singapore.

62. I. K. MacKenzie, T.L. Khoo, A. D. McDonald, B. T. A. McKee, Phys. Rev. Lett. **19**, 946 (1967).

63. W. Brandt, H. F. Waung, P. W. Levy, Proc. Intern. Symp. Rome, p. 48, (1968).

64. I. Y. Dekhtyar, M. I. Dekhtyar, V. V. Dyakin, F.A. Zaitov, Sov. Phys. Semicon. **18**, 1230 (1984).

65. R. Krause-Rehberg, H. S. Leipner, Positron Annihilation in Semiconductors, Defect Studies, Springer Series, New York.

66. I. Prochazka, Materials Structure, **8**, 2 (2001).

67. P. Kirkegaard, N. J. Pedersen, M. Eldrup,: In Positron annihilation.

68. C. Hubner, J. Gebauer, H. S. Leipner, R. Krause-Rehberg, unpublished results (1997b).

69. C. Hubner, T. Staab, R. Krause-Rehberg, Appl. Phys. A **61**, 203 (1994)

70. Y. Nishi, T. Miyata, J. Nomoto, and T. Minami, Proc. of the 37th IEEE Photovoltaic Specialists Conference, Seattle, WA, 2011 (IEEE, New York, 2011).

71. A. Mittiga, E. Salza, F. Sarto, M. Tucci, and R. Vasanthi, Appl. Phys. Lett. **88**, 163502 (2006).

72. J. Kansy, *Nucl. Instr and Meth*. *A* **374**, 235 (1996).

73. K. Hinode, S. Tanigawa, and M. Doyama, *J. Phys. Soc. Jpn.* **41**, 203 (1976).

74. C. Dauwe, M. Dorikens, L. Dorikens-vanpraet, and D. Segers, *Appl. Phys.* **5**, 117 (1974)**.**

75. T. Hoshino, N. Papanikolaou, R. Zeller, P. H. Dederichs, M. Asato, T. Asada, and N. Stefanou, *Comp. Mater. Sci.* **14**, 56 (1999).

76. L. C. Smedskjaer, M. J. Fluss, D. G. Legnini, M. K. Chason, and R. W. Siegel, *J. Phys. F: Metal Phys.* **7**, 1715 (1977).

77. J. Xue and R. Dieckmann, *J. of Phys. Chem. Solids* **51**, 1263 (1990).

78. D. Wu, Q. Zhang, and M. Tao, *Phys. Rev. B* **73**, 235206 (2006).

79. S. Åsbrink and L. J. Norrby, *Acta Crystallogr*. *B* **26**, 8 (1970).

80. G. K. Paul, Y. Nawa, H. Sato, T. Sakurai, and K. Akimoto, *Appl. Phys. Lett.* **88**, 141901 (2006).

81. M. Clement, J. M. M. de Nijis, P. Balk, H. Schut, and A. van Veen, *J. Appl. Phys.* **79**, 9029 (1996).

82. J. Gebauer, R. Krause-Rehberg, S. Eichler, M. Luysberg, H. Sohn, and E. R. Weber, *Appl. Phys. Lett.* **71**, 638 (1997).

83. P. Asoka-Kumar, M. Alatalo, V. J. Ghosh, A. C. Kruseman, B. Nielsen, and K. G. Lynn, *Phys. Rev. Lett.* **77**, 2097 (1996).

84. T. Chiba, J. Chem. Phys. 64 (1976) 1182.

85. J. Bloem, Philips Res. Repts. **13**, 167, 1958.

86. David O. Scanlon, Kate G. Godinho, Benjamin J. Morgan, and Graeme W. Watson, J. Chem. Phys. **132**, 024707 (2010).

87. Xilang nie, Su-Huai, and S. B. Zhang, Phys. Rev. Lett. **88**, 066405 (2002).

88. O. Porat and I. Riess, Solid State Ionics, **74**, 229 (1994).

89. J. A. Van Vechten, Handbook on Semiconductors, p. 36 (1980).

90. J. Schmit and A. A. Lucas, Solid. State. Commun. 11, 415 (1972).

91. J. A. Van Vechten, Phys. Rev. B **7**, 1479 (1973).

92. J. A. Van Vechten, Phys. Rev. **182**, 891 (1969).

93. J. A. Van Vechten, Phys. Rev. **187**, 1007 (1969).

94. J. C. Philips, J. A. Van Vechten, Phys. Rev. B **2**, 2147, (1970).

95. J. A. Van Vechten, Phys. Stat. Sol. (b) **47**, 261 (1971).

96. R. D. Shannon, Acta Crystallogr. Sect. B **24**, 388 (1968).

97. M. Sasaki and M. Shimode, J. Chem. Solids **64**, 1675 (2003).

98. O. Crottaz and F. Kubel, Z. Kristallogr. **211**, 481 (1996).

99. Mandeep Singh, B. R. Mehta, Deepak Varandani and V. N. Singh, J. Appl. Phys. **106**, 053709 (2009).

100. Kiran Singh, Bohdan Kundysl, Maria Poienar and Charlessimon, J. Phys.: Condens. Matter **22**, 445901 (2010).

101. J. Pellicer-Porres, A. Segura, D. Kim , Semicond. Sci. Technol. **24**, 015002 (2009).

102. Otfried Madelung, Semiconductors : Data handbook (Springer, 3rd edition, 2004).

103. K. G. Godinho, B. J. Morgan, J. P. Allen, D. O. Scanlon and G. W. Watson, J. Phys.: Condens. Matter **23**, 334201 (2011).

BIOGRAPHICAL INFORMATION

Ameena Fnu, received her Bachelor's degree of science from Vanitha Mahavidyalaya Hyderabad, from India in 1997, Master of Science in physics in 1999 from Hyderabad Central University India. To pursue her Ph.D in physics she started her graduate study at University of Texas in Arlington in 2004 and received Master of Science degree in Physics in 2007. She joined the Photovoltaics group headed by Dr. Michael Jin in August 2007. She earned a Doctor of Philosophy in Applied Physics in May 2012 under the guidance of Dr. Michael Jin.